



HAL
open science

Design and performance of a modular combined cycle solar power plant using the fluidized particle solar receiver technology

Omar Behar, Benjamin Grange, Gilles Flamant

► To cite this version:

Omar Behar, Benjamin Grange, Gilles Flamant. Design and performance of a modular combined cycle solar power plant using the fluidized particle solar receiver technology. *International Journal of Energy Conversion and Management*, 2020, 220, pp.113108 -. 10.1016/j.enconman.2020.113108 . hal-03523225

HAL Id: hal-03523225

<https://univ-perp.hal.science/hal-03523225>

Submitted on 27 Jun 2022

HAL is a multi-disciplinary open access archive for the deposit and dissemination of scientific research documents, whether they are published or not. The documents may come from teaching and research institutions in France or abroad, or from public or private research centers.

L'archive ouverte pluridisciplinaire **HAL**, est destinée au dépôt et à la diffusion de documents scientifiques de niveau recherche, publiés ou non, émanant des établissements d'enseignement et de recherche français ou étrangers, des laboratoires publics ou privés.



Distributed under a Creative Commons Attribution - NonCommercial 4.0 International License

1 **1. Introduction**

2 The development of the Solarized Gas Turbine (SGT) and the associated combined cycles
3 has attracted a lot of interest in recent years because it is one of the ways (with supercritical
4 cycles) to improve solar to electric efficiency.

5 Initially, very small (micro) SGT have been developed as an alternative to Stirling engines
6 integrated to solar dish collector using turbocharger technology [1, 2]. Next, a concept with
7 dedicated GT has been developed within the framework of the OMSOP project for producing
8 an efficient, reliable, and cost-effective system that can generate about 3 - 25 kW [3, 4].

9 However, solar dish technologies have not been fully deployed to the market yet [5]. This is
10 due to technical issues of scale-up, lack of thermal energy storage solution, and high
11 investment costs associated with solar dish technology. Thus, R&D activities have been re-
12 oriented to the improvement of central receiver technology. The latter is easier to scale up and
13 already reached sizes above 100 MW. Besides, it promises to be one of the most viable
14 renewable options to replace fossil fuel power generation technologies in the near future [6].

15 Indeed, the integration of the GT cycle to the solar central receiver system was demonstrated
16 at both small and pre-commercial scales. Research projects including SOLGATE [7-9],
17 SOLHYCO [10], and SOLUGAS [11-12] have tested and proved the concept of SGT. Heller
18 et al. [7-9] have reported the results of the SOLGATE project, which aimed to investigate the
19 feasibility of operating SGT at the hundred-kilowatt scale. During this project, a 250 kW gas
20 turbine was powered using three solar air receivers, connected in series, to heat the
21 compressed air up to 800-1000°C. The SOLGATE SGT was operated for 135 h including
22 about 96 h of on-sun tests. SOLHYCO project aimed at the development and demonstration
23 of a SGT-cogeneration system able to operate in both solar and hybrid modes. A 100 kW GT
24 has successfully tested during a period of more than 165 hours. The main objective of
25 SOLUGAS was the qualification and validation of the first SGT at the pre-commercial scale

1 (megawatt-scale). Thus, a 4.6 MW gas turbine has been modified to integrate a pressurized air
2 receiver. The compressed air has been extracted from the compressor to be preheated by a 3.2
3 MW_{th} solar air receiver up to 800°C [11-12]. The compressed air is then injected into the
4 combustion chamber to reach the turbine inlet temperature (TIT). The SOLUGAS SGT was
5 operated during one year under a wide range of conditions, including a standard working
6 regime for commercial plants [11].

7 The cited projects have successively proved the SGT with pressurized air receiver at both
8 experimental and pre-commercial scales. Following these projects, various studies have
9 further investigated the performance of the SGT. Behar [12] proposed to preheat the
10 compressed air of the SGT using parabolic trough technology. The simulation showed that a
11 solar to electric efficiency of 17% is achievable. Bellos et al. [13] used a multi-objective
12 approach to optimize the SGT with a parabolic trough technology. The analysis showed that
13 the optimum design leads to 64% fuel savings but with 2.8% penalty on the produced
14 electricity. Spelling [14] used a multi-objective optimization approach to evaluate the thermo-
15 economic performance of several configurations of the SGT. The author concluded that the
16 integration of thermal energy storage and the use of combined-cycle configurations are
17 mandatory to overcome the limitations of the simple-cycle SGT. Grange et al. [15]
18 investigated the impact of packed bed energy storage on the performance of SGT with
19 pressurized air receiver. Simulations showed that the use of a packed bed heat storage allows
20 increasing the solar fraction by 10-15%. Sánchez-Orgaz et al. [16] investigated the impact of
21 the recuperator effectiveness in a multi-step SGT. The authors pointed out that for the
22 optimum design the increase in the effectiveness of the recuperator is always associated with
23 an increase in the overall efficiency of the SGT. Santos et al. [17] developed a modular
24 thermodynamic model for predicting the performance of the SGT. Based on the model
25 developed by previous authors, Merchán et al. [18] have evaluated the annual performance of

1 several configurations and operation modes of a SGT with pressurized air receiver. The
2 authors analyzed the margin for improvement for each component and concluded that the
3 Brayton cycle is the key element to improve the overall efficiency. Petrakopoulou et al. [19]
4 have investigated the integration of a SGT with a high-temperature air volumetric receiver.
5 The results showed that the significant amount of solar energy required to increase the inlet
6 temperature of the combustion chamber to 800-1000 °C causes a relative decrease in the
7 energy efficiency of the SGT.

8 The previous scientific literature review highlights the limitations of the use of pressurized air receiver including
9 low thermal efficiency, low allowable solar heat flux, and limited working temperature..
10 Besides, the use of air as a heat transfer fluid (HTF) is associated with unsolved issue about
11 thermal energy storage, which results in limited capacity factor and solar share and daily start-
12 up and shut-down of the SGT. This induces a significant increase in the O&M costs and cost
13 of the electricity produced.

14 The use of particles as a HTF was introduced to improve the thermal efficiency of the solar
15 receiver, to increase the working temperature (allowing high allowable heat flux), and to
16 integrate efficient and cost-competitive thermal energy storage. Up to now, there are three
17 promising concepts of solar particle receivers. The first one is the so-called falling particle
18 receiver, which is developed by Sandia Laboratory (SNL) [20]. The second concept is the
19 centrifugal receiver, which is developed by the German aerospace center (DLR) [21]. The
20 third one, known as particles-in-tube (or dense suspension of particles) solar receiver, has
21 been developed by CNRS within the framework of the CSP2 [22] and Next-CSP [23]
22 European projects. This concept relies on a simple-proven design [24, 25]. The main
23 advantages are the use of a tube-receiver similar to the standard receiver of solar power tower
24 and small diameter particles that exhibit high wall-to-fluidized bed heat transfer [26].

25 The review of the previously published studies showed that there are few published works on
26 the SGT with fluidized particle receiver. Farsi and Dincer [27] have conducted a

1 thermodynamic analysis of a solar power plant with a fluidized particle receiver. They
2 concluded that the integration of the particle solar receiver with direct energy storage in the
3 Rankine and Brayton cycles enables to achieve the energy and the exergy efficiencies of 50%
4 and 53.8% respectively. Kang et al. [28] have carried out the energy analysis of a hybrid solar
5 combined cycle with particles-in-tube solar receiver and direct energy storage. The authors
6 indicated that the overall efficiency of the thermal conversion (without the optical part) might
7 achieve 48%. An attempt to evaluate the LCOE (Levelized Cost Of Electricity) of modular
8 solar tower plants using solid particles as Heat Transfer Media (HTM), allowing HTM
9 temperatures up to 1000°C is proposed in [29]. A LCOE of about 6 c€/kWh is found for high
10 insolation site like in Chile. The previous cited works proposed a simplified analysis of some
11 parts of the SGT and did not account for the actual performance of the SGT at part-load.
12 Besides, the practical design of the solar receiver and the heliostat field for a given capacity of
13 the GT is not investigated. The design of some components such as the multi-stages fluidized
14 bed heat exchanger and the steam cycle were arbitrary selected rather than designed based on
15 practical approach. This study proposed a complete approach that fills the gap between purely
16 academic approaches and detailed engineering developments providing a realistic design tool
17 that integrates comprehensive modeling of each component. Moreover, from the academic
18 point of view, this work establishes a methodology for the modeling of complex solar thermal
19 energy conversion systems that integrate components modeled on the basis of optical, thermal
20 science, and thermodynamic concepts.

21 Reliable simulation tools are needed to predict the performance of large-scale solarized gas
22 turbine cycles with a particles-in-tube solar receiver and direct storage of particles. Therefore
23 providing a flexible approach necessary to upscale the technology to a commercial level,.

24 The present work aims at designing and evaluating the performance of a solar gas turbine
25 combined cycle with a fluidized particles-in-tube receiver and direct thermal storage using

1 practical modeling techniques. We propose the design of a representative medium-scale
2 module using an on-the-shelf gas turbine. Section 2 describes the modeling approaches while
3 section 3 provides the design and the validation of each component of the system. Section 4
4 and 5 present the performance evaluation during typical days and under different operation
5 strategies. The most important conclusions are summarized in the last section.

6 **2. Modeling the components of the system**

7 **2.1. Description of the system**

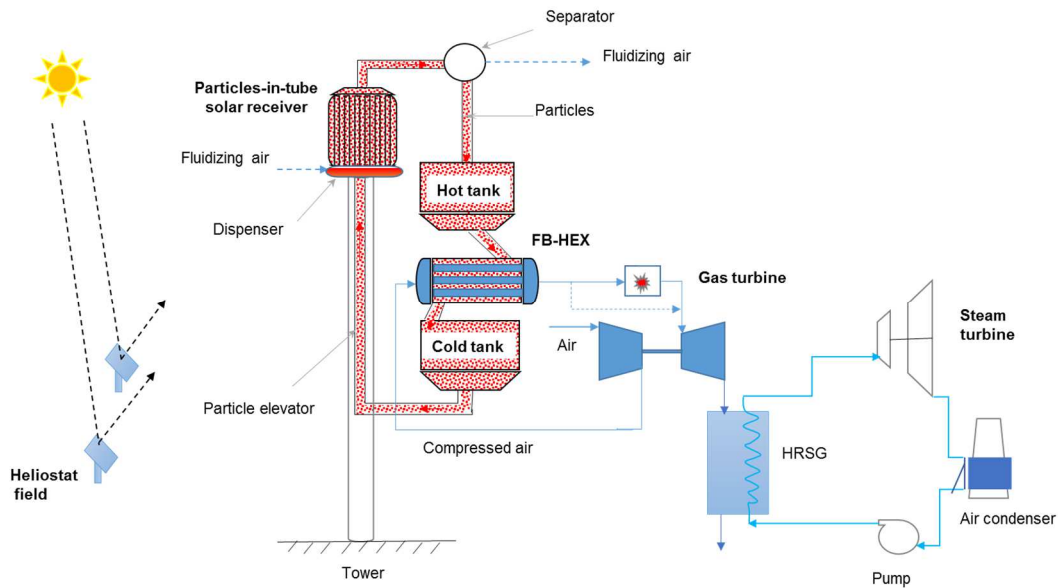
8 Figure 1 shows a typical solar gas turbine combined cycle with a fluidized particles-in-tube
9 receiver and direct thermal storage. It consists of four main sub-systems:

- 10 • The heliostat field,
- 11 • The solar particle receiver,
- 12 • The two-Tank particle storage and fluidized particles/pressurized air heat exchanger,
- 13 • The combined-cycle integrating a modified simple cycle GT and a Rankine steam
14 cycle.

15 During sunny periods, the particles flow from the cold tank toward the receiver where they
16 are heated up in tubes. The particles circulate upward inside the tubes in the fluidized state
17 (fluidization with air). Then they are stored in the hot tank. When power production is needed,
18 they are introduced in a fluidized bed heat exchanger to heat the compressed air of the GT.
19 The GT can work in two modes: hybrid solar-fuel mode and solar-only mode. In solar-only
20 mode, the compressed air is heated into the FB-HEX and then passes directly in the turbine
21 section where it expands. In the case of hybrid mode, the compressed air is preheated in the
22 FB-HEX and flows in the combustion chamber to be heated up to reach the turbine inlet
23 temperature (TIT). The exhaust gases of the GT passes through a Heat Recovery Steam
24 Generator (HRSG) to produce superheated steam for the Rankine cycle.

25

1
2
3



4

Figure 1. Solar gas turbine combined cycle with particle-in-tube-receiver and direct thermal storage

5

6 The complete design started with the solar gas turbine (SGT) since it defines the necessary

7

8 power to run it. Then, the other parts have been designed upstream. However, to make this

9

10 section easier for the readers, it is organized into three main sub-sections starting from solar

11

12 energy collection to power production.

13

- Modeling of the solar field and the particles-in-tube solar receiver,
- Modeling of the fluidized bed heat exchanger,
- Modeling of the simple gas turbine cycle.

14

15 The model of the steam cycle is given in Appendix A.

16

17 The main assumptions used in the modeling are as follows:

18

- Each component is at steady state during each time-step;

19

- The start-up and shut-down losses are ignored;

20

- The temperature in the cold and hot tanks is uniform as well as in each stage of the

21

fluidized bed heat exchanger;

22

fluidized bed heat exchanger;

23

fluidized bed heat exchanger;

24

- 1 - The absorber surface of the solar cavity receiver is flat, tube shape is not taken into
- 2 account;
- 3 - The tower shadow is neglected.

4 **2.2. Modeling of the heliostat field and the particle-in-tube solar receiver**

5 The models of the solar field and the receiver are presented together because they are strongly
 6 linked. The solar field is designed using SolarPILOT, a software from NREL [30], with a
 7 design power, depending on the desired particle outlet temperature (750°C or 880°C).

8 The cavity receiver consists of absorber tubes at the back positioned on a curved line when
 9 looking at the top view. The tube number and geometry are detailed in section 3.3. The cavity
 10 is made of five refractory panels and the aperture has a 5.5 m height and a 6 m width, with an
 11 angle of 20° relative to the vertical plane.

12 To avoid any deterioration of the receiver due to uneven flux distribution leading to thermal
 13 hot spots and unacceptable stresses [31], an aiming point strategy is applied using the
 14 heliostats location optimized in SolarPILOT. This strategy is based on the TABU search [32]
 15 combined with the convolution-projection method Unizar [33] and is applied at the aperture
 16 of the receiver to spread the flux density on the tubes and reduce the maximum flux density.

17 The heliostat locations, their aiming point, and the receiver geometry are introduced as input
 18 in the ray-tracing software Solstice [34] to get the flux distribution on the absorber tubes.

19 The flux map on each receiver surface (cavity and absorber) is introduced into a thermal
 20 model based on the net radiation method [35]. This method relies on the radiative balances in
 21 the infrared spectrum.

$$22 \quad E_i^{IR} = \varepsilon_i \cdot \sigma \cdot T_i^4 + \rho_i^{IR} \cdot \left(\sum_j F_{ij} \cdot E_j^{IR} \right) \quad (1)$$

23 With F_{ij} the view factor from the surface i to the surface j .

24 The radiative balance in the solar spectrum is achieved by the ray-tracing SOLSTICE
 25 software. The net power absorbed by the element i is given by,

$$\dot{Q}_i^{solabs} = A_i \cdot (\dot{q}_i^{sol} + \sum_j F_{ij} \cdot E_j^{IR} - E_i^{IR}) \quad (2)$$

With \dot{q}_i^{sol} the solar incident flux density after the radiative balance in the solar spectrum (W/m²).

The surface heat transfer from the front wall to the particles is calculated by the following equation,

$$\dot{q}_{tr} = h_{tr}(T_{front} - T_{part,mean}) \quad (3)$$

With h_{tr} the heat transfer coefficient (W/m².K), T_{front} the front wall temperature (K) and $T_{part,mean}$ the mean particle temperature between the inlet and the outlet (K).

Small-fluidized particles, typically 50 μ m mean diameter, are used as heat transfer fluid in the receiver tubes. The heat transfer coefficient, h_{tr} , was selected based on experimental results with a single tube achieved at the 1-MW solar furnace at the CNRS-PROMES laboratory [24, 25].

The particle flow rate is adjusted to reach the desired particle outlet temperature. Simulations are carried out for different sun positions. Then, interpolation is used to find the appropriate particle temperature and flowrate for a given sun position.

2.3. Modeling of the FB-HEX

Typical FB-HEX is a multi-stages tube/shell heat exchanger, in which the compressed air of the GT flows into the tubes [36]. The fluidized particles in the shell-side flow from higher temperature stages to lower temperature stages. The energy balance on one stage of a FB-HEX can be expressed as,

$$Q_{particles} = Q_{working_air} + Q_{fluidizing_air} \quad (4)$$

With,

$$Q_{particles} = m_{particles}(h_{particles_in} - h_{particles_out}) \quad (5)$$

$$Q_{working_air} = m_{working_air}(h_{working_air_out} - h_{working_air_in}) \quad (6)$$

$$Q_{fluidizing_air} = m_{fluidizing_air}(h_{fluidizing_air_out} - h_{fluidizing_air_in}) \quad (7)$$

1 where Q , m , and h are the energy, the mass flow rate and the enthalpy respectively, subscript
 2 “working_air” refers to the compressed air of the GT, “fluidizing_air” refers to the air used to
 3 fluidize the particles, “in” and “out” refer to the inlet and outlet of the HEX’s stage
 4 respectively. The FB-HEX is supposed to be well-insulated and installed in-door so that in
 5 Equation (4) the heat losses to the ambient are neglected. The outlet temperature of the
 6 fluidizing air is supposed to be equal to that of the particles.

7 The heat gained (per unit of tube length) by the working air can be calculated by,

$$8 \quad Q_{working_air} = \pi \times D_{tube_inner} \times U_{working_air} (T_{tube_inner} - T_{working_air_average}) \quad (8)$$

9 D_{tube_inner} is the inner diameter of the HEX’s tubes and $U_{working_air}$ is the heat transfer
 10 coefficient of the working air. It is calculated using Gnielinski correlation [37].

$$11 \quad Nu_{working_air} = \frac{(F_{friction}/2) \times (Re - 1000) \times Pr}{1 + 12.7 \sqrt{(F_{friction}/2)} \left(\frac{2}{Pr^{3/4} - 1} \right)} \left(\frac{Pr}{Pr_{tube}} \right)^{0.11} \quad (9)$$

12 where Nu is Nusselt number, $F_{friction}$ is the friction coefficient, Re is Reynolds number, and Pr is
 13 Prandtl number.

14 Similarly, the heat released by the particles can be given as,

$$15 \quad Q_{particles} = \pi \times D_{tube_outer} \times U_{particles} (T_{particles_average} - T_{tube_outer}) \quad (10)$$

16 Where: D_{tube_outer} is the outer diameter of the HEX’s tubes and $U_{particles}$ is the heat transfer
 17 coefficient between the particles and the tubes (a value of $800 \text{ W/m}^2\cdot\text{K}$ is considered in this
 18 study), and $T_{particles_average}$ is the mean temperature of the particles.

19 The tube outer surface temperature (T_{tube_outer}) is calculated based on energy conservation on
 20 the tubes of the HEX. The conduction heat transfer, per unit of length, from the tube outer
 21 surface to the tube inner surface is,

$$22 \quad Q_{conduction_tube} = 2\pi \times k_{tube} \frac{(T_{tube_inner} - T_{tube_outer})}{\ln\left(\frac{D_{tube_outer}}{D_{tube_inner}}\right)} \quad (11)$$

1 The tube inner surface temperature is calculated by combining equations (6) and (11) while
 2 the working fluid outlet temperature is calculated by combining Equations (6) and (8). The
 3 particle outlet temperature is calculated by combining Equations (6) and (10).
 4 The above model is used to predict the performance of one stage of the FB-HEX. Combining
 5 N stages in series results in a multi-stages FB-HEX.

6

7 **2.4. Modeling the gas turbine cycle**

8 The typical GT cycle consists of a compressor, a combustion chamber, and a turbine section.

9 A practical technique, based on the performance maps of the turbine and compressor sections,

10 has been used to model the GT cycle. This approach enables to predict the turbine

11 performance for part-load operations, based on similarity and dimensional analyses, and is

12 widely used in turbomachinery [38]. Indeed, the maps are graphical representations of the

13 performance of the components (compressor and turbine sections) for a given set of operating

14 conditions [39], which are themselves expressed in terms of certain corrected variables with

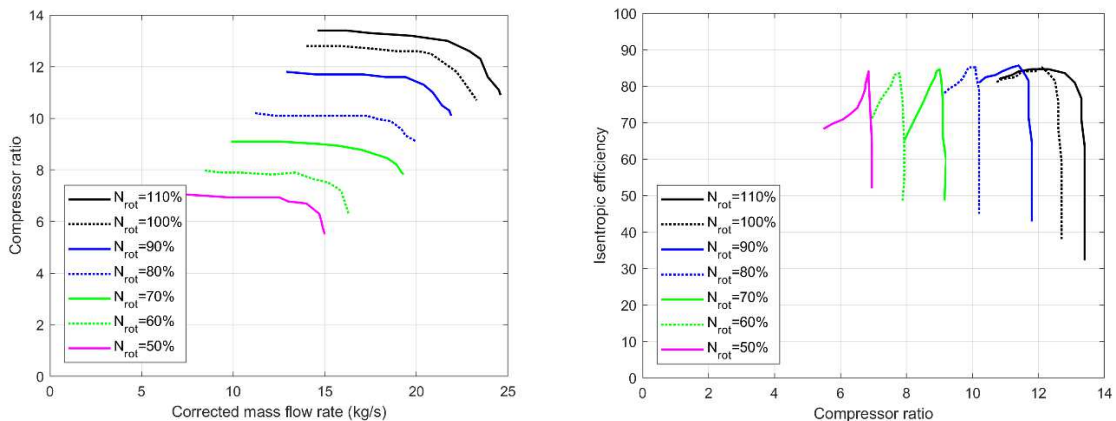
15 respect to reference inlet pressure and temperature (15°C, 1 atm.). For the compressor, the

16 maps provide the compressor ratio and isentropic efficiency as a function of the corrected

17 mass flow and corrected shaft speed. For the turbine section, the maps provide isentropic

18 efficiency and expansion ratio as a function of the same parameters. Figure 2 represents the

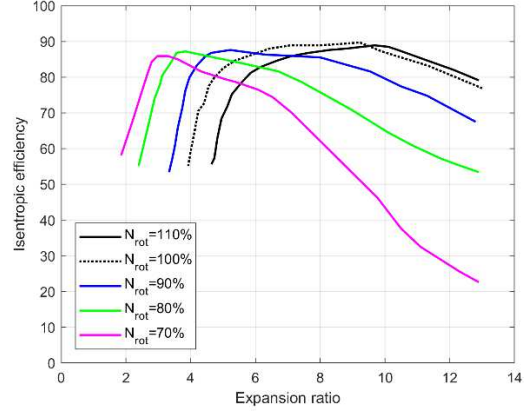
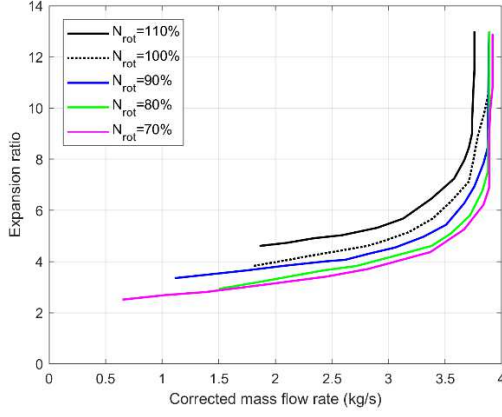
19 components' maps of a typical gas turbine unit.



20

1

(a)



(b)

2
3

4

Figure 2. Performance maps of typical gas turbine unit: (a) compressor: compressor ratio and isentropic

5

efficiency, (b) turbine: expansion ratio and isentropic efficiency [Adapted from ref. 38].

6

Based on the inlet parameters of the compressor, the corrected shaft speed (N_{cor_C}) and

7

corrected mass flow rate (m_{cor_C}) are respectively given by,

$$8 \quad N_{cor_C} = \frac{N_{rot}}{\theta_C} \quad (12)$$

$$9 \quad m_{cor_C} = m_{air} \frac{\theta_C}{\alpha_C} \quad (13)$$

10

The index ‘‘C’’ refers to the compressor. θ_C and α_C are non-dimensional factors defined as,

$$11 \quad \theta_C = \sqrt{\frac{T_{C_in}}{T_{STD}}} \quad (14)$$

$$12 \quad \alpha_C = \frac{P_{C_in}}{P_{STD}} \quad (15)$$

13

The index ‘‘in’’ refers to the compressor inlet. P_{STD} and T_{STD} are respectively the pressure and

14

temperature under standard conditions.

15

The compression ratio and isentropic efficiency of the compressor are functions of the

16

corrected mass flow rate and the corrected shaft speed.

1 $\delta_C = f(N_{cor_C}, m_{cor_C})$ (16)

2 $\eta_s^C = f(N_{cor_C}, m_{cor_C})$ (17)

3 The following relation provides the exit air temperature of the compressor for isentropic
4 process.

5 $T_{C_out_s} = T_{C_in} (\delta_C)^{\frac{\gamma_C - 1}{\gamma_C}}$ (18)

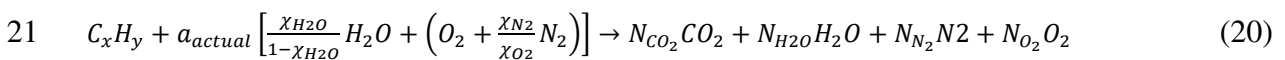
6 In order to calculate the actual outlet temperature of the compressor, the following definition
7 of isentropic efficiency is used.

8 $\eta_s^C = \frac{h_{C_out_s} - h_{C_in}}{h_{C_out} - h_{C_in}}$ (19)

9 The same methodology is developed to model the turbine section. To match the compressor
10 and turbine characteristics, the actual turbine mass flow is compared to the compressor mass
11 flow and the fuel mass flow. An iteration process on the compressor mass flow is applied to
12 find the operation point.

13 It is worth noting that a closed cooling system is considered, in which a fraction of
14 compressed air is extracted for cooling the turbine blade. This cooling air is then mixed with
15 the exhaust gases at the outlet of the turbine section. The modeling of the cooling system in
16 this study is based on the model developed in [40].

17 The combustion process in the gas turbine involves the fuel (the hydrocarbon) and the
18 oxidizer (air) called the reactants, which undergo a chemical process while releasing heat to
19 form the products of combustion such that mass is conserved. Thus, the chemical reaction can
20 be expressed as follows,



1 a_{actual} is the actual air coefficient, χ_x and N_x represent the fractions and the number of moles
2 respectively.

3 The combustion chamber outlet temperature is calculated based on the following equation,

$$4 \quad T_{CC_outlet} = \frac{[(m_{\text{working_air}} - m_{\text{cooling_air}})C_{P_{CC_inlet}}T_{CC_in} + m_{\text{fuel}}Q_{cv}\eta_{cc} + m_{\text{fuel}}C_{P_{\text{fuel}}}T_{\text{fuel}}]}{[(m_{\text{working_air}} - m_{\text{cooling_air}} + m_{\text{fuel}})C_{P_{CC_outlet}}]} \quad (21)$$

5 $m_{\text{cooling_air}}$ is the mass flow rate of the air that is used to cool the turbine blade, subscript CC
6 refers to the combustion chamber, m_{fuel} and T_{fuel} are the mass flow rate and the temperature of
7 the fuel respectively, η_{cc} is the combustion efficiency, and Q_{cv} is the fuel calorific value.

8 **3. Design of the components**

9 The design of the components has been carried out as follows. First, an off-the-shelf gas
10 turbine that is able to work in both hybrid and solar-only modes was selected. Next, the
11 fluidized bed heat exchanger was designed with appropriate temperature-approach. The
12 number of stages of the FB-HEX was determined based on the temperature approach and with
13 respect to the design cold temperature of the particles (the temperature at the outlet of the FB-
14 HEX). The receiver-loop, comprising the receiver, the storage, and the heliostat field, was
15 then sized to meet the heat demand of the GT cycle. Finally, the steam cycle was designed
16 based on the exhaust gases' parameters of the GT cycle. A flowchart showing the main design
17 steps of the complete system is given in Appendix A.

18 The system is supposed to be installed in Ouarzazate Province in the Drâa-Tafilalet region of
19 south-central Morocco, at an elevation of 1100 m, in the middle of a bare plateau south of the
20 High Atlas Mountains. The coordinates of the site are 31°N and 6.86°W. During the night, an
21 ambient temperature of 15°C and a relative humidity of 60% are considered.

22 **3.1. Design data and validation of the GT model**

23 Table 1 illustrates the design data of the selected gas turbine. Siemens GT-500 17 MW-gas
24 turbine [41] was chosen because it is suitable and available for the first commercial SGT with

1 a fluidized particles-in-tube solar receiver. Low TIT and high power/weight ratio are the most
 2 important advantages of GT-500 with respect to the solar application. The former leads to
 3 optimum performance when the GT is working in solar-only mode.

4 Table 1. Design data of Siemens SGT-500 [41]

Design data	Value	Unit
Compressor		
Compressor ratio	12	-
Isentropic efficiency (assumed)	0.91	-
Combustion chamber		
Pressure losses (assumed)	4	%
Turbine Inlet Temperature (TIT)	850	°C
Combustion efficiency	0.99	-
Turbine section		
Isentropic efficiency (assumed)	0.92	-
Gas turbine unit		
Nominal shaft speed	3600	rpm
Nominal output (under standard conditions)	17	MWe
Mechanical efficiency	99	%
Electrical efficiency	99	%

5
 6 It is worth noting that components' performance maps are subject to confidentiality because it
 7 is the core of the GT design. Thus, the maps have been up-scaled and adapted based on those
 8 published in the literature. The practical technique used to model the GT is driven by the
 9 actual operations of the GT. The technique leads to find the operation point of the gas turbine
 10 as a function of ambient conditions and turbine load. To validate the GT model, the predicted
 11 results are compared with the rig-tests published performance [41].

12 Figure 3 illustrates a comparison between the predicted performance and Siemens' rig-tests
 13 data, for the case of the heat rate and the electricity generation, as a function of compressor
 14 inlet temperature. Good agreement has been observed thanks to components' maps, which
 15 consider the effect of ambient temperature on the compressor/expansion ratios as well as on
 16 the isentropic efficiencies of the compressor and turbine sections.

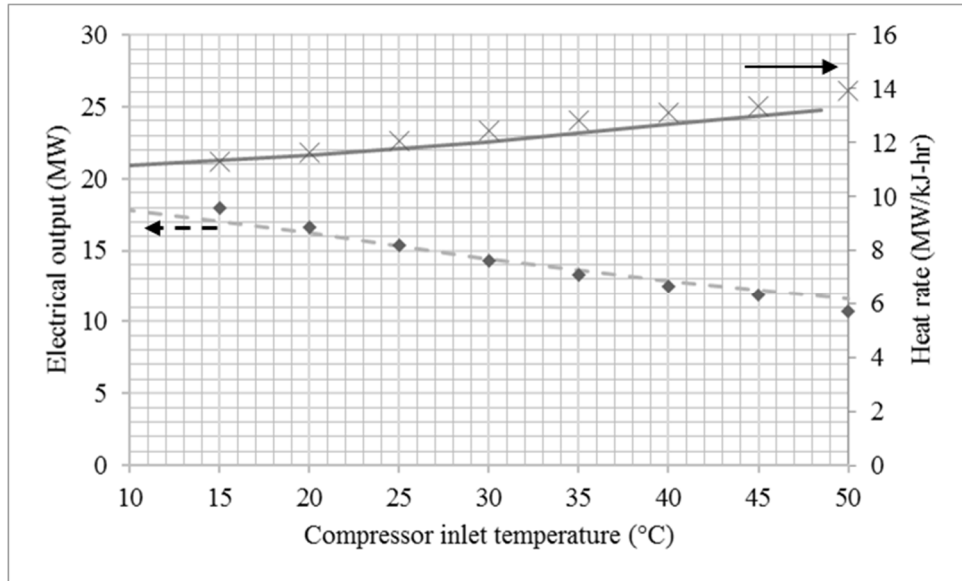


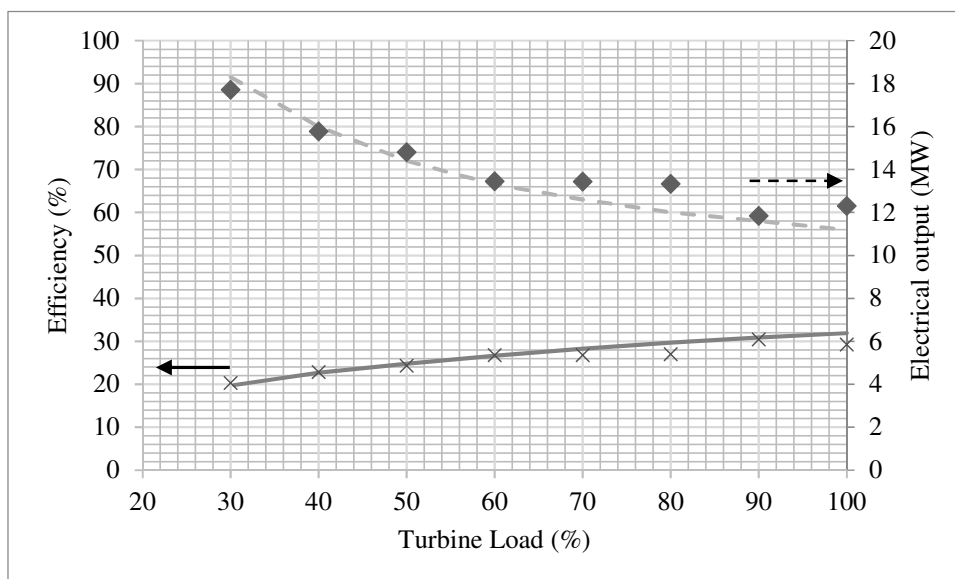
Figure 3. Electrical output and heat rate as a function of compressor inlet temperature (lines are Siemens data, points are model predictions)

As shown in Table 2, there is a minor difference between predicted performance and Siemens' rig-tests data. For the generated power, the Mean Absolute Deviation (MAD) is about 0.44 MW, which corresponds to difference of 3.4%. The deviation in the prediction of the heat rate is also negligible. The percentage is 3.3%, which corresponds to a MAD of 418 kJ/kWh. Accurate results have also been obtained for the case of the mass flow rate and the temperature of the exhaust gases. For the former, the mean deviation is 3.46% and for the latter, it is less than 1.55 %.

Table 2. Statistics for the validation of the gas turbine model

Operation mode	Parameter	Mean Absolute Deviation	Percentage of MAD (%)
Full-load	Power generation	0.44 [MW]	3.43
	Heat rate	0.42 [MJ/kW-hr]	3.30
	Exhaust gasses mass flow	2.72 [kg/s]	3.46
	Exhaust gasses temperature	6.04 [°C]	1.54
Part-load	Heat rate	0.61 [MJ/kW-hr]	4.76
	Efficiency	1.07 [%]	3.74

1 The potential of the GT model to predict the part-load performance was examined because it
 2 is of particular interest for optimum planning of the GT operations. Figure 4 illustrates a
 3 comparison between the predicted performance and Siemens rig-tests data, for a wide range
 4 of turbine load, from 30% to 100%. For instance, at 30% load, rig-tests efficiency is 20.27%
 5 and the corresponding predicted value is 20.32%. The accurate predictions are obtained
 6 thanks to the practical technique adopted to model the gas turbine. Indeed, the model takes
 7 into account the shaft speed. For each given load and taking into account the ambient
 8 conditions, the model finds the appropriate shaft speed and matches the compressor and the
 9 turbine sections to produce the desired power. Thus, the MAD for the part-load performance
 10 is minor. It is 4.76% for the heat rate and only 3.74% for the efficiency.
 11 These data confirm the potential of the model to predict both the full-load and the part-load
 12 performance of the gas turbine. The slight deviation of the gas turbine model is strongly
 13 related to unknown specific design details of the Siemens GT-500 that are not available. The
 14 uncertainties in the correlations used to estimate the thermo-physical properties of gases have
 15 a second-order impact.



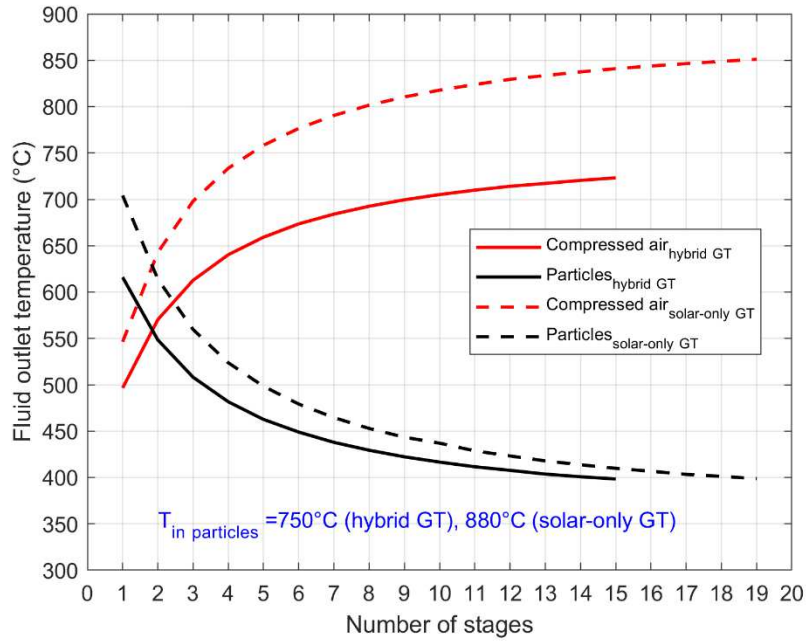
16
 17 **Figure 4.** Electrical output and efficiency as a function of turbine load (the line is Siemens data, points are
 18 model predictions)

1 **3.2. Design of the FB-HEX**

2 To design the FB-HEX, the inlet parameters of the particles and the compressed air must be
3 defined first. The nominal inlet parameters of the compressed air correspond to the nominal
4 outlet parameters of the compressor. For the hybrid case, particles at a nominal inlet
5 temperature of 750°C is considered, because it is the state-of-the-art based on the past
6 experimental results [42]. In the solar-only design, the nominal inlet temperature of the
7 particles is supposed to be 880°C. This value is selected based on the TIT and the temperature
8 approach of the FB-HEX.

9 The FB-HEX is then designed and the number of stages is determined based on a temperature
10 approach of 30°C. The particle temperature at the outlet of the FB-HEX is fixed at 400°C to
11 keep the particles working within the technical specifications (manufacturer technical data).

12 A sensitivity analysis through varying the number of stages is carried out to find the
13 appropriate number of stages that meet the specifications cited above. Figure 5 indicates that
14 the appropriate number of stages for the hybrid design is 15 stages while it is 19 stages for
15 solar-only design. The effect of the number of stages on the outlet temperatures of the
16 compressed air is presented in Figure 5 to provide a comprehensive analysis. It is apparent
17 that the higher the number of stages, the higher the outlet temperature of the compressed air
18 and the lower the outlet temperature of the particles because the increase in the number of
19 stages increases the heat transfer area. Nevertheless, the higher the number of stages, the
20 lower is the temperature increase in the high-temperature stages due to the decrease in the
21 heat transfer coefficient (HTC). Besides, the difference in the HTC between the first stage and
22 the last stage for the case of solar-only is 21%. Consequently, 15-stages FB-HEX provides an
23 appropriate temperature approach (27°C) for the solar-only case.



1
2
3
4
5
6
7
8
9
10
11

Figure 5. Effect of the number of stages on the performance of the FB-HEX.

Table 3 illustrates the design data of the FB-HEX for the hybrid and solar-only GTs. The difference between the compressor mass flow rate in the hybrid case and the solar-only case is related to the pressure drop. For solar-only, the combustion chamber is by-passed (100% solar-powered), which reduces the pressure drop and consequently the mass flow rate increases. The pressure drop in the FB-HEX (pressurized-air side) is higher in the case of solar-only GT than in the case of hybrid GT because of the increase in the operating temperature.

Table 3. Nominal design data of the FB-HEX

Parameter	Hybrid GT	Solar-only GT	Unit
Compressor mass flow rate	79.445	80.73	kg/s
Compressor outlet temperature	340	341.58	°C
Compressor outlet pressure	10.07	10.06	bar
Particles inlet temperature	750	880	°C
Particles outlet temperature	398	399.87	°C

Particles mass flow rate	82	79.9	kg/s
Length of the stage	0.5	0.5	m
Number of stages of the FB-HEX	15	19	-
Heat transfer area	3958.4	5014	m ²
Nominal pressure drop (pressurized air)	188.4	271.0	mbar

1

2 3.3. Design of the heliostat field and the solar receiver

3 After the design of the FB-HEX, the solar field's components have been designed including
4 tower, receiver, and heliostats. The tower height is set to 120 m and the heliostats have a
5 reflective surface of 49 m² (7 m x 7 m) with a reflectance of 92% and a slope error of 0.9
6 mrad (high optical quality). The total reflective surface of the heliostat field is 77 518 m² and
7 126 812 m² for the hybrid and solar-only GT, respectively. In the latter case, the heliostat field
8 is larger because a constant particle mass flow rate for both cases is considered. The third case
9 (called "Solar-only GT – Low flowrate" in this paper) consists of keeping the solar field of
10 the hybrid case and decreasing the particle mass flow rate to reach a particle outlet
11 temperature of 880°C. The three considered cases have the same tower height and receiver
12 geometry. Table 4 illustrates the main design data of the three considered cases.

13

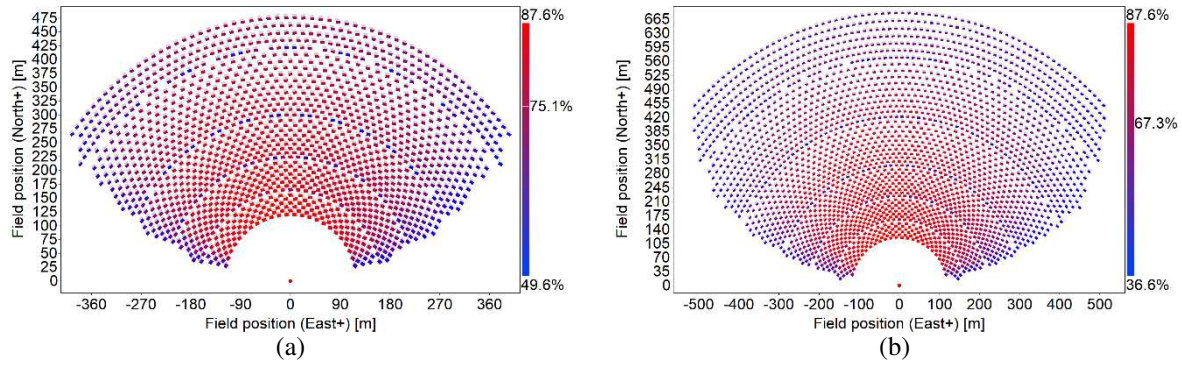
Table 4. Main design data of the three considered operation modes

Case	Hybrid GT	Solar-only GT	Solar-only GT – Low flowrate
Tower height (m)	120		
Heliostat field (m ²)	77 518	126 812	77 518
Hot temperature of particles (°C)	750	880	880
Receiver geometry	382 tubes of 7 meters height and an outer diameter of 50 mm		

14

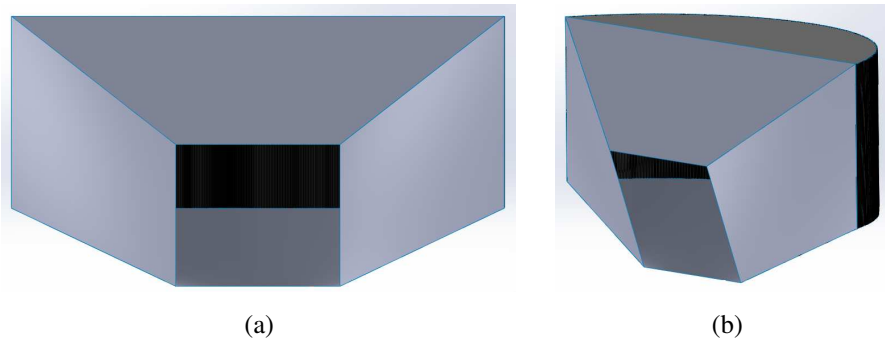
15 The layouts of the heliostat field for the hybrid and solar-only GTs are presented in Figure 6.

16 The layout of the heliostat field of the third case is similar to that of hybrid GT.



1 **Figure 6.** Layout of the heliostat field optimized in SolarPILOT with associated nominal optical efficiency for
 2 (a) Hybrid GT (1582 heliostats) and (b) Solar-only GT (2588 heliostats).

3 The wide shape of the heliostat field is voluntary due to the geometry of the receiver shown in
 4 Figure 7. Indeed, Eastern and Western heliostats are required to reach the side absorber tubes.



5 **Figure 7.** View of the solar receiver – (a) Front view, (b) 3D view

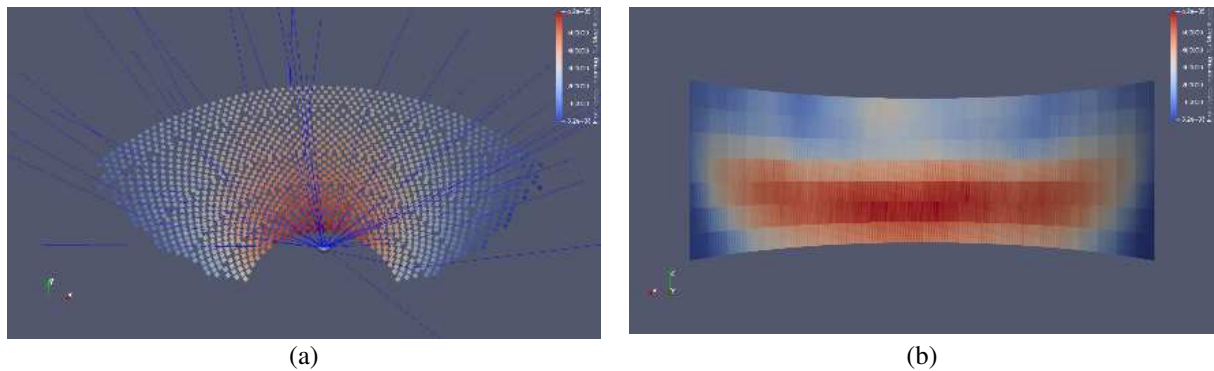
6 The solar receiver consists of 382 tubes of 7 meters height and with an outer diameter of
 7 50 mm (black surface in Figure 7). With a nominal mass flowrate in the receiver of 90 kg/s
 8 and assuming a uniform distribution of particle in the tubes, it leads to a mass flow rate per
 9 unit surface area per tube of around 60 kg/m².s. This value lies in the range experimentally
 10 validated in [18]. The cavity is made of five refractory panels. The optical properties of the
 11 tubes and the panels are given in Table 5.

12 **Table 5.** Optical properties of the tubes and refractory panels

Parameter	Tubes	Refractory Panels
Emissivity (-)	0.85	0.93
Absorptance (-)	0.9	0.2

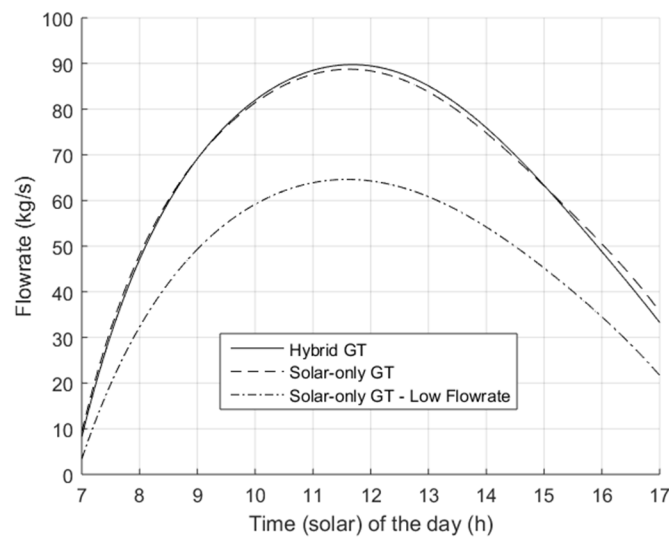
13

1 Figure 8 shows the results of the ray-tracing simulation with Solstice displayed in Paraview
 2 for the reference hybrid case (vernal equinox at noon) with the DNI value from Ouarzazate.



3 **Figure 8.** Results of Solstice displayed in Paraview for the hybrid case – (a) heliostat field (color code: cosine
 4 efficiency), (b) absorber (color code: flux density in W/m²)

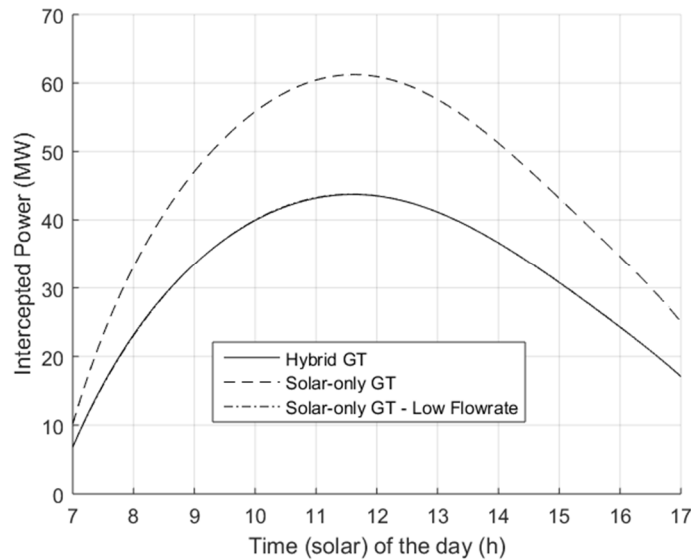
5 The maximum flux density on the absorber tubes is 620 kW/m² and 806 kW/m² for the hybrid
 6 and solar-only cases respectively. Figures 9, 10 and 11 present, respectively, the evolution of
 7 the particle mass flow rate, the intercepted power, and the optical and thermal efficiency
 8 during the 21st of March, for the three cases. All the results are shown in solar time.



9
 10 **Figure 9.** Particle mass flowrate during the 21st of March for the three studied cases

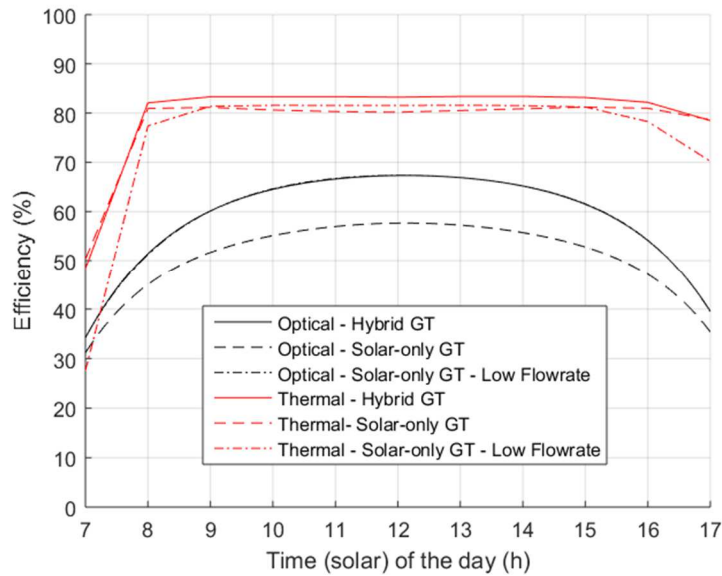
11 The particle mass flowrate follows the same evolution during the day for the hybrid GT and
 12 solar-only GT. It reaches a maximum value of 65 kg/s for the solar-only GT-low flowrate and
 13 90 kg/s for the other two cases. The intercepted power (power entering the receiver aperture)

1 varies with the daytime from 6.8 MW to 44 MW for the hybrid GT (and for the solar-only
2 GT-low flowrate) and from 10.1 MW to 61.6 MW for the solar-only GT.



3
4 **Figure 10.** Intercepted power during the 21st of March for the three studied cases

5 The tradeoff made on the aperture between the spillage loss and the thermal efficiency leads,
6 at solar noon, to an optical efficiency of 67.4% (12.9% of the optical losses come from the
7 spillage) and a thermal efficiency of 83.2% for the hybrid GT. For the solar-only GT, the
8 optical efficiency drops down to 57.6% with 20.8% of spillage loss, and the thermal
9 efficiency is 80.2%. The optical efficiency of the third case follows the same trend as the
10 hybrid case. The thermal efficiency is maintained around 80% during the day.

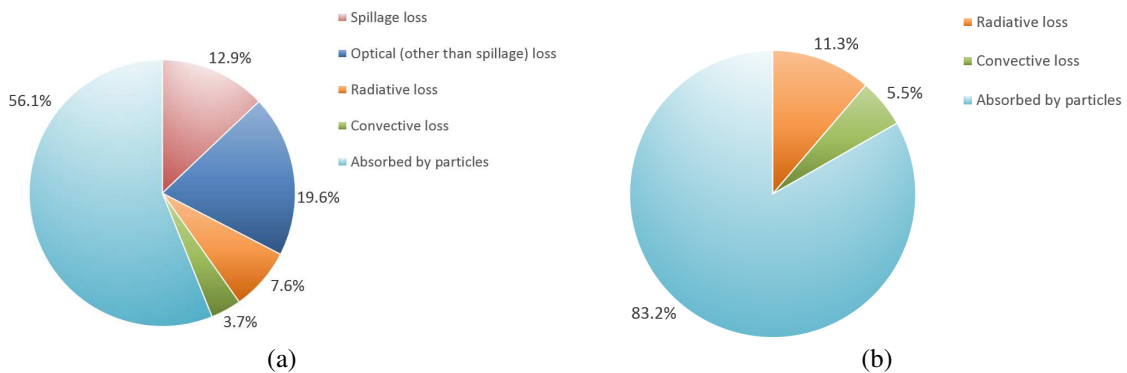


1
2
3
4
5
6

Figure 11. Optical and thermal efficiency during the 21st of March for both hybrid and solar GT

The low thermal efficiency at 7 AM is due to a low particle mass flowrate because of a DNI of only 256 kW/m².

At nominal conditions, the power balance is given in Figure 12.



7
8

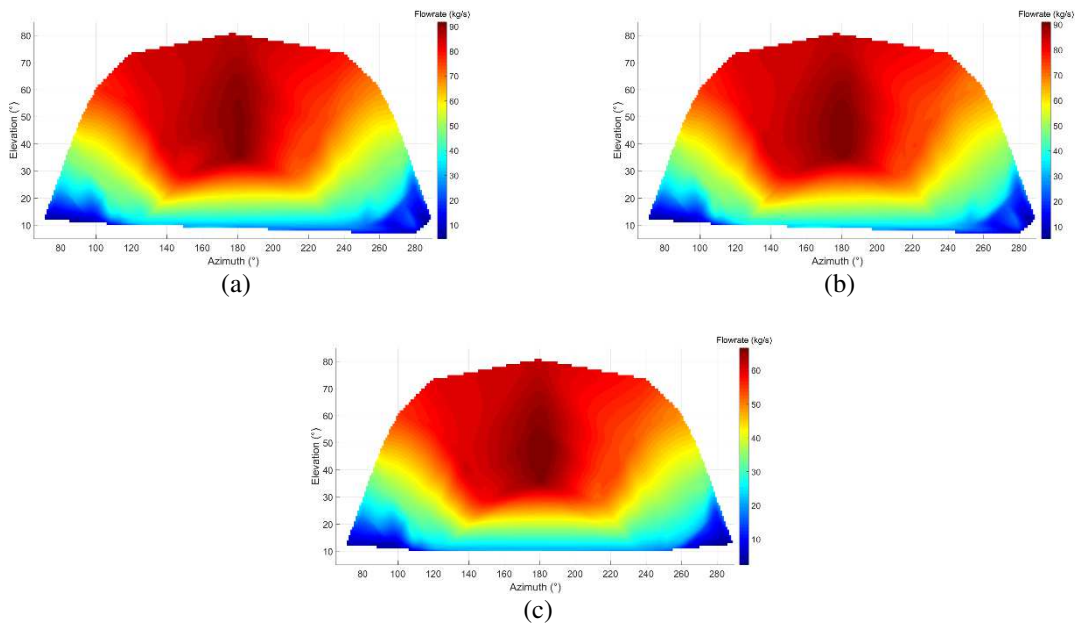
Figure 12. Power balance on the solar receiver (hybrid case) the 21st of March at noon (a) with optical loss (b) only thermal loss

9 Table 6 shows the amount of hot particles collected during the vernal equinox and the
10 winter/summer solstices and the equivalent full-load operation duration for the three cases
11 given in Table 4. The amounts collected during summer solstice corresponds to the maximum
12 storage capacity of the plant. Compared to the vernal equinox, there are around 15% less
13 particles collected at the winter solstice and around 3% more particles at the summer solstice.

1 Table 6. Amount of hot particles collected during the vernal equinox and the winter/summer solstices and
 2 equivalent full-load operation duration (see Table 3)

	Winter Solstice	Vernal Equinox	Summer Solstice
Hybrid GT (T particle at 750°C)	2027 t	2432 t	2510 t
Solar GT (T particle at 880°C)	2060 t	2431 t	2494 t
Equivalent full-load operation duration (round numbers)	7.1 h	8.4 h	8.6 h
Solar GT (T particle at 880°C) – Low flowrate	1440 t	1730 t	1766 t
Equivalent full-load operation duration	5 h	6 h	6.1 h

3
 4 Simulations are then carried out for different sun positions during the year, the 21st of each
 5 month. Simulations before 8 AM and after 4 PM are performed if the DNI (average hourly
 6 DNI over the month) is higher than 150 W/m² (below this value the particle mass flow rate is
 7 too low to gain power from the wall). Between 8 AM and 4 PM, simulations are achieved
 8 every two hours with an average hourly DNI throughout the year. Then, the results are
 9 interpolated as a function of the sun azimuth and elevation. Figure 13 shows the interpolation
 10 of the particle flowrate for three cases as a function of the sun position.



11 **Figure 13.** Particle mass flowrate versus sun position– (a) Hybrid GT, (b) Solar-only GT, (c) Solar-only GT –
 12 Low flowrate

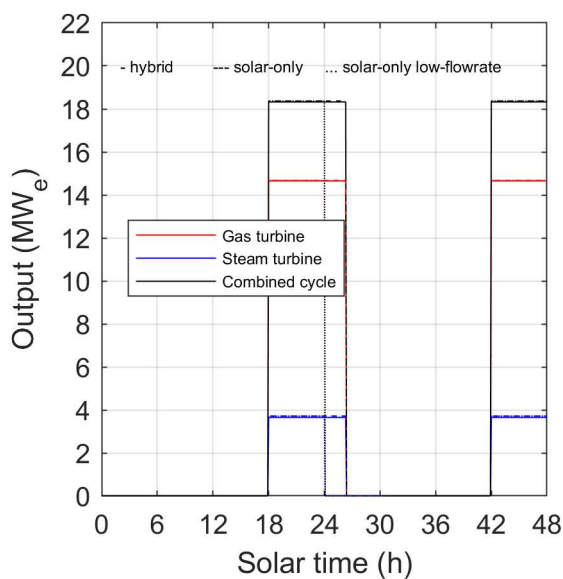
1 Similar to Figure 9, the amount of hot particles collected at any sun position is quite similar
2 for the first two cases. For the third case, the amount of hot particles collected corresponds to
3 approximately 70% of the amount collected in the first two cases.

4 **4. Performance evaluation of the complete power plant**

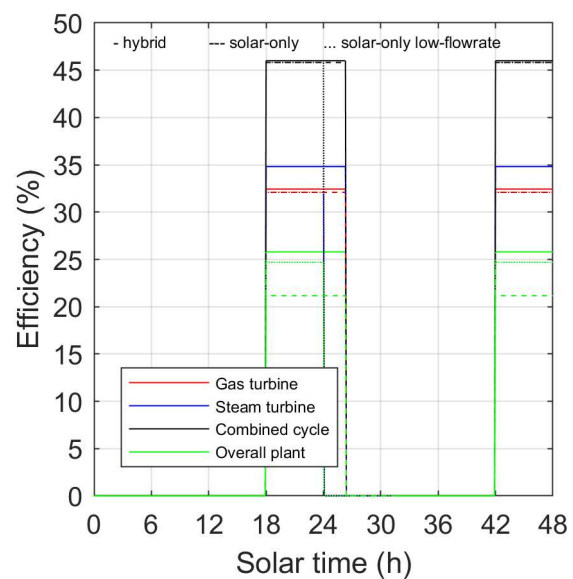
5 The previous sections described the design and performance of the system's components
6 including GT, FB-HEX, solar receiver, and solar field. For the steam cycle, the design and
7 performance are given in Appendix B. The present section describes the performance of the
8 complete power plant (illustrated in Figure 1). A flowchart showing the main steps of the
9 methodology used to calculate the performance of the complete system during typical period
10 is given in Appendix A. The performance metrics used to evaluate the plant are the power
11 output, the efficiency, the solar share, the specific fuel consumption, and the capacity factor.
12 Two operation strategies are considered: constant power production after 18h and constant
13 power production on demand. This means that the solar plant is operated as a peaker.

14 Figure 14 shows the power production and the thermal efficiency of the thermodynamic
15 cycles during 21-22 March, for the three cases (hybrid, solar-only, and solar-only low-
16 flowrate), operating in a constant power production strategy after 18 pm, at the site located in
17 Ouarzazate. The GT cycle produces about 14.7 MW instead of 17 MW (output under STD
18 conditions) because of the high elevation of the site (1100 m). The operation duration for the
19 case of solar-only low-flowrate is shorter than for the other two cases because of the low
20 amount of the particles in the storage (see Table 6). The slight difference in the CC power
21 production between the solar-only case and hybrid case is related to the air mass flow of the
22 GT's compressor (see Table 3). Indeed, the compressor air mass flow of hybrid GT is slightly
23 lower than that of solar-only GT (79.445 vs. 80.73 kg/s) because of the difference in the
24 pressure drop. However, the decrease in the pressure drop pushes the operation point of solar-
25 only GT far further from the nominal point, compared with that of the hybrid GT, which

1 results in additional efficiency losses, as plotted in Figure 14b. The thermal efficiency of the
 2 GT cycle for the cases of hybrid and solar-only are 32.09 % and 32.43%, which corresponds
 3 to an output of 14.67 MW and 14.65 MW respectively. The steam turbine efficiency is the
 4 same for the three cases (34.82%) leading to a generation of 3.72 MW. Thus, the CC output
 5 reaches about 18.37 MW for the three cases with 46% efficiency. The overall efficiency (also
 6 known as solar-to-electric efficiency) is the product of the individual efficiencies of the
 7 heliostat field, the receiver, and the CC. The results illustrated, in green color, in Figure 14b
 8 corresponds to the product of the full-load efficiencies. The overall efficiency of the hybrid
 9 case is 25.80%. This value decreases to 24.70% for the case of solar-only low flowrate due to
 10 the slight decrease in the thermal efficiency of the solar receiver (from 83.2% for the hybrid
 11 case to 80%). For the solar-only case, the overall efficiency is 21.16%, which is 4.64 points
 12 lower than that of the hybrid case. This is mainly due to the low optical efficiency of the
 13 heliostat field, which drops from 67.4% (for the hybrid case) to 57.6% for the case of the
 14 solar-only. The decrease in the thermal efficiency of the receiver has a second-order impact
 15 (83.2% for the hybrid case vs. 80.2% for the solar-only case).



(a)

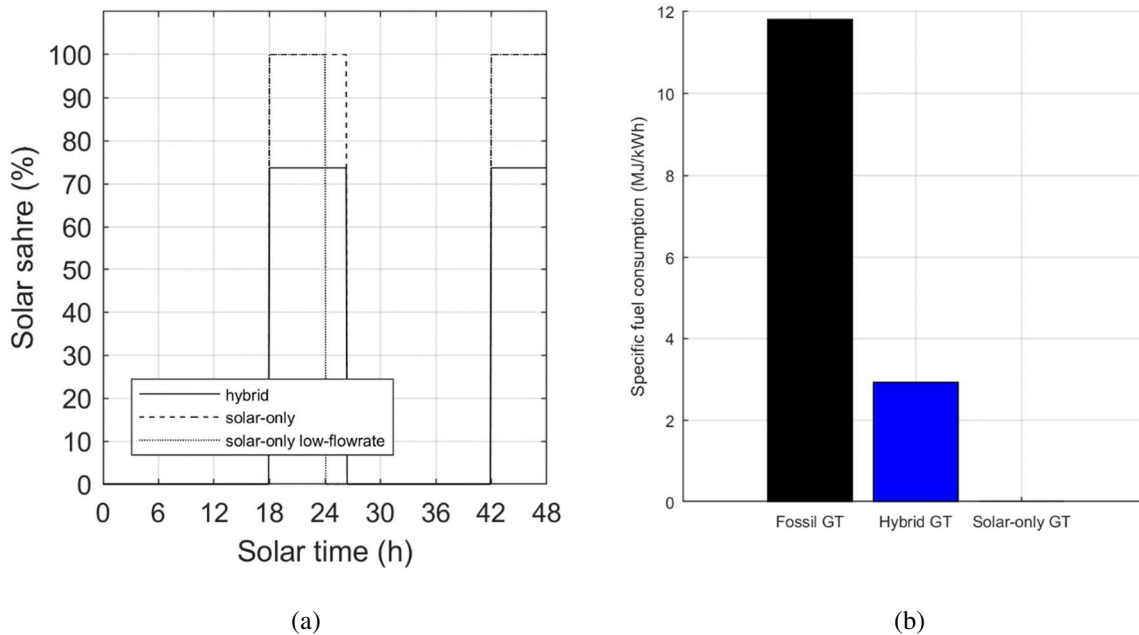


(b)

16

1 **Figure 14.** Power production and efficiency the power block during the 21st-22^{ed} March operating with a
 2 constant power production after 18 pm

3 Figure 15a shows the solar share for the three cases. The solar share of the two solar-only
 4 cases is 100%, which means no fuel is used. For the hybrid case, an additional amount of fuel
 5 is required to reach the TIT. The solar share for the hybrid GT is 73.70%, which results in low
 6 Specific Fuel Consumption (SFC), as shown in Figure 15b. The use of solar energy in the
 7 hybrid case allows reducing the SFC from 11.29 MJ/kWh (for the case fossil fuel GT) to 2.92
 8 MJ/kWh in hybrid GT.



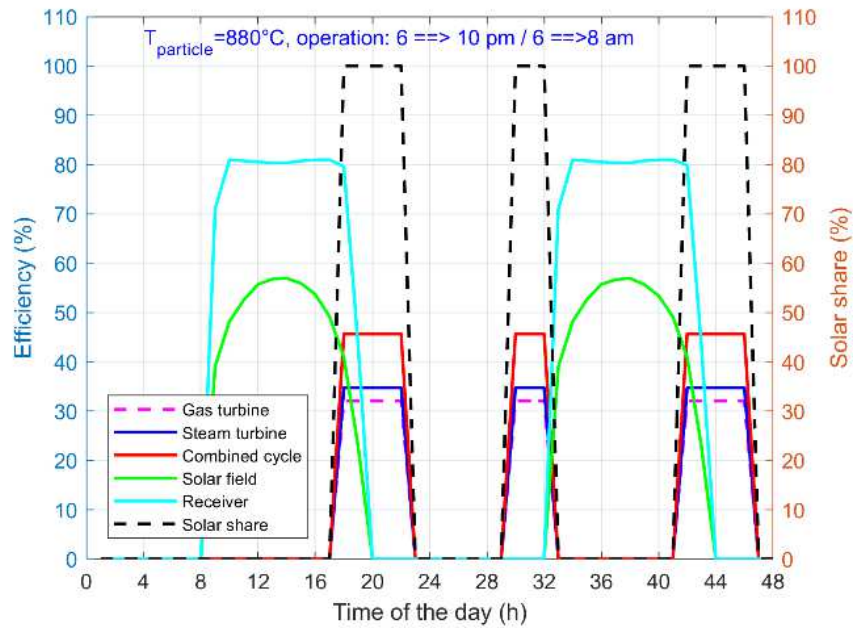
9

10 **Figure 15.** (a) Solar share of the three studied cases (left) and (b) specific fuel consumption of the GT (right)

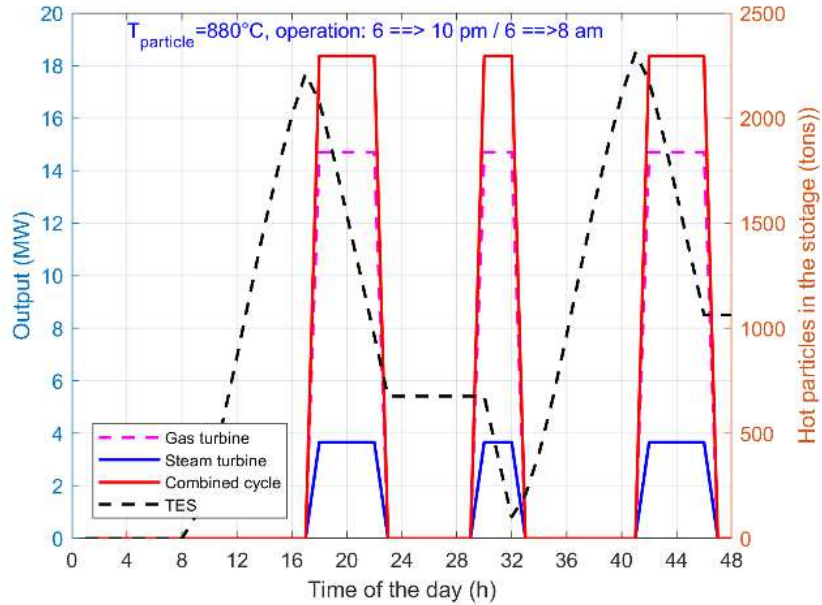
11 The proposed solar power plant is modular because of its medium size. Moreover, several
 12 solar collection loops (the tower and the receiver) can be associated in parallele to increase the
 13 total power and the storage capacity of the plant. In this option, the nominal power of the
 14 combined cycle shared by the solar collection loops will increase proportionally.

15 Thanks to the thermal energy storage the system offers great flexibility for saving solar
 16 energy and generatind power when needed. Figure 16 shows the performance of each
 17 component for the case of solar-only operating to meet a constant power need during the

1 periods of peak demand (18 pm-22 pm, then 6 am-8 am). The efficiency of the components
 2 (including heliostat field, receiver, and power conversion cycles) during 21-22 March is
 3 presented in Figure 16a. The power production and the state of the TES are given in Figure
 4 16b. Flexible power production management is possible to meet a given objective. Particles
 5 can be stored during a day (8 am to 18 am) to be used when needed (18 pm-22 pm, then 6 am-
 6 8 am). Besides, the remaining energy in the storage can be saved to the next days, as shown in
 7 Figure 16b. The proposed concept is flexible enough to store energy for the next days. For
 8 instance, particles can be stored to meet the peak demand of a rainy day, which can be
 9 forecasted even one week before.



(a)



(b)

1

2 **Figure 16.** Efficiencies and solar share (a), power production and state-of-the-storage (b) of solar-only combined
 3 cycle operating on-demand

4 Figure 17a shows the amount of electricity generated during the vernal equinox and the
 5 winter/summer solstices. The operation strategy is a constant power production after 18h. The
 6 operation duration for the case of solar-only low flowrate is short according to the amount of
 7 particles in the storage (see Table 5). Figure 17b illustrates the seasonal and annual capacity
 8 factor of the three cases. Solar-only and hybrid cases have the same storage capacity so that
 9 they have the same capacity factor. During summer, the capacity factor can reach 35.83%.
 10 This value corresponds to the maximum capacity factor of the plant and it is 10 points higher
 11 than that of solar-only low flowrate case. Interestingly, the capacity factor during spring
 12 (autumn is similar to spring) is almost similar to that of summer for the three studied cases
 13 (the difference is less than 1%). The average capacity factor during winter is just 5 points
 14 lower than that of equinox. As a result, the annual capacity factor can reach 33.47% for hybrid
 15 and solar-only cases, and 23.75% for the case of solar-only low flowrate.

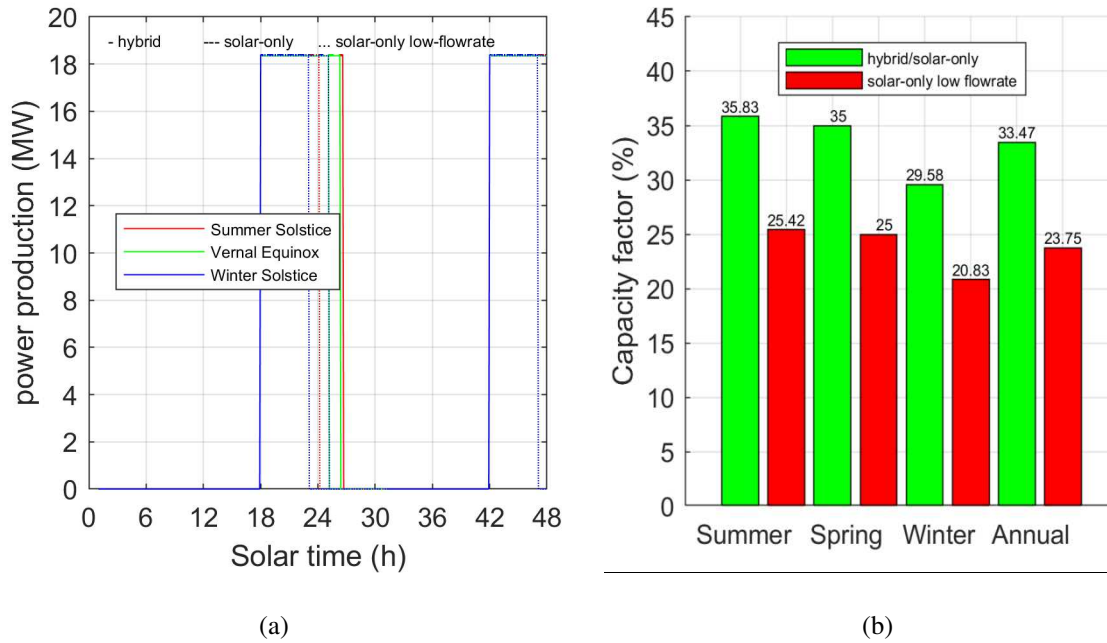


Figure 17. Seasonal operation duration (left) and capacity factor (right) of the three studied cases

5. Off design performance of a solarized gas turbine

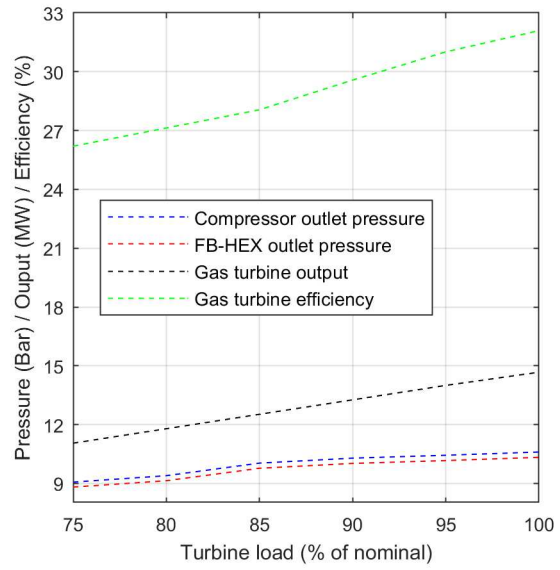
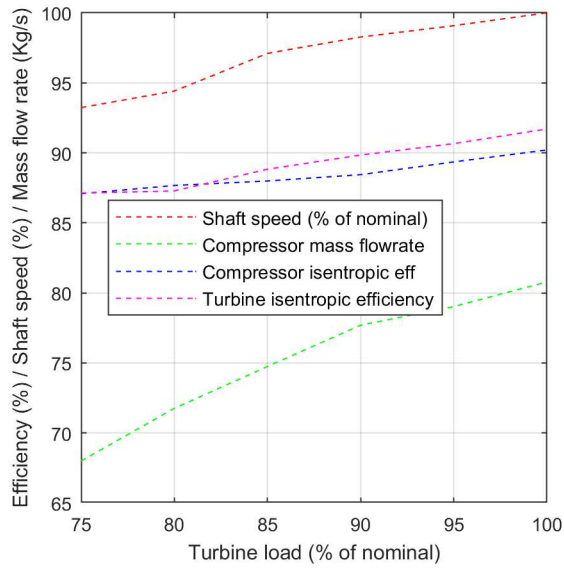
This section focuses on the part-load performance of a solarized gas turbine. Because of the similarity, the case of solar-only is considered as an example. The selected operation strategy consists of keeping the particles mass flow rate at its nominal value and reducing the power production of the GT. Consequently, the GT is subjected to the variation in the compressor mass flow rate associated with the variation of TIT. Figure 18 shows the performance of the GT as a function of the generated power (percentage of nominal load). The load of the GT is reduced from 100% to 75%. This is done by reducing the shaft speed of the GT to a value that corresponds to the desired amount of electricity produced. As Figure 18a demonstrates, a slight decrease in the shaft speed (from its nominal value) results in a significant loss in the GT performance. By reducing the GT load from 100% to 75%, the isentropic efficiency of the compressor and the turbine section is significantly reduced from its nominal value (90%, and 91.7% respectively) to 87%, which represents 5% losses. The mass flow rate of the compressor is the most affected parameter. It decreased from 80.79 kg/s, at the nominal point, to 68 kg/s, at 75% load, which represents a cut of 16%. This results in a reduction in the

1 pressure at the compressor outlet. Therefore, the pressure drop in the FB-HEX declines (low
2 mass flow rate results in low Reynolds number). As Figure 18b illustrates, the compressor
3 outlet pressure decreases from 10.6 bar to 9.06 bar, which corresponds to a 14.5% loss. The
4 diminution in the FB-HEX outlet pressure is 14.7%. As can be seen in Figure 18c, at 75%
5 turbine load, the pressure drop is reduced from 271 mbar to 253 mbar (6.5% decrease).

6 At partial load, the outlet temperature of the compressor drops due to the decline in the outlet
7 pressure. As shown in Figure 18d, the compressor outlet temperature is reduced from 341°C
8 to 324°C. However, the TIT raises from 850°C to 876°C (but remains acceptable from the
9 safety point of view) thanks to the selected operation strategy that kept the particles mass flow
10 rate in the FB-HEX constant. Nevertheless, the FB-HEX is also affected by the partial load
11 operations. When the turbine load declines from 100% to 75%, the temperature of the
12 particles at the outlet of the FB-HEX raises from 399.38°C to 442°C, because of the low
13 compressor air mass flow rate.

14 Another important point to mention is the turbine outlet temperature, which increases at
15 partial load. This is due to the combined effect of low turbine inlet pressure (due to low
16 compressor outlet pressure) and losses in the isentropic efficiency. The former results in a low
17 expansion ratio while the latter induces additional entropy generation so that the turbine outlet
18 temperature increases.

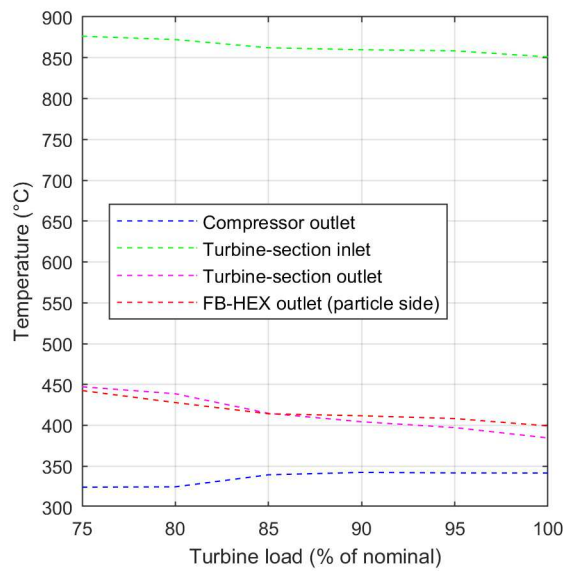
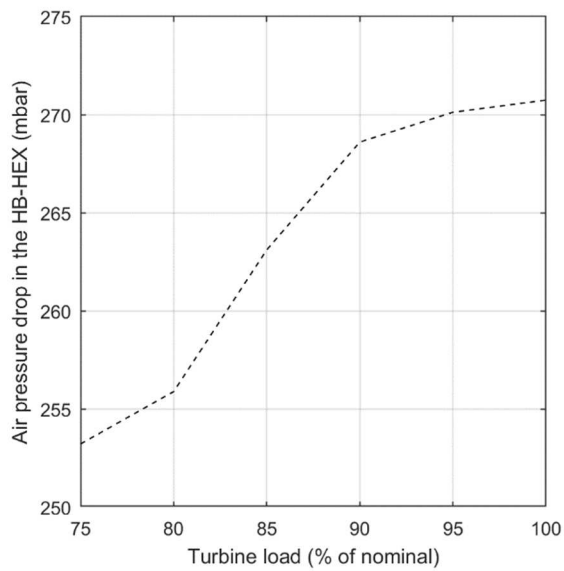
19 Table 7 summarizes the losses in the performance of each part of the solarized gas turbine. As
20 can be noticed, all the parts are penalized at partial load. As a result, there are significant
21 losses in the overall efficiency. When the turbine load reduces to 75%, the GT efficiency loses
22 6 points (from 32% to 26%), which represents a decrease of 18.4%.



1

(a)

(b)



2

(c)

(d)

3

Figure 18. Part load performance of solarized gas turbine (case of solar-only)

4

Table 7. Losses in the performance of the solarized gas turbine at part load (percentage of nominal

5

performance)

Turbine Load	Losses in shaft speed	Losses in compressor isentropic efficiency	Losses in turbine isentropic efficiency	Losses in overall efficiency
75%	6.76	3.46	14.48	18.37
80%	5.58	2.81	11.39	15.48
85%	2.89	2.45	5.33	12.57
90%	1.73	1.95	2.95	7.86
95%	0.92	0.94	1.56	3.37

1 The analysis of the performance of the three studied cases (hybrid, solar-only, and solar-only
2 low flowrate) shows that the performance of the solar part (heliostat field and receiver) has a
3 critical influence on the overall performance of the solar power plant. In other words, the
4 increase in the operating temperature of the receiver does not obviously improve the overall
5 efficiency of the complete power plant. This fact can be observed when comparing the hybrid
6 case with a solar-only low flowrate case (high operating temperature of the receiver reduces
7 the overall efficiency by 4.26%). Besides, the high operating temperature of the receiver
8 requires a large heliostat field (the case of solar-only), which is associated with a low optical
9 efficiency (large heliostat field has decreased the overall efficiency from 25.80% to 21.16%,
10 which represents a loss of 18%). Even though high operation temperature increases the
11 efficiency of the thermodynamic cycle, it induces a decrease in the thermal efficiency of the
12 solar receiver. On the other hand, the high operating temperature of the receiver requires a
13 large solar field, which decreases the optical efficiency. The overall efficiency is the product
14 of the three cited efficiencies and further studies should identify the optimum operating
15 temperature of the receiver that maximizes the overall efficiency of the complete solar power
16 plant.

17 **6. Discussion**

18 The proposed solar power plant offers significant improvements in the thermal efficiency with
19 respect to the state of the art even using an off-the-shelf gas turbine. Furthermore, the
20 designed solar part (solar field and solar receiver) can be considered as a representative
21 module of larger plants that associate several modules sharing the same power block (heat
22 exchanger and combined cycle). 100 MW and more solar power plants can be designed on
23 this basis provided an additional study on particle conveying between the towers and the
24 power block. An increase of cycle efficiency from 46% to 48.8% is expected for commercial-
25 scale solar power plants [43].

1 However, there is room for additional improvement using sCO₂ cycles that enables 50% cycle
2 efficiency and more with 750°C particle temperature and solar-only operation. For example,
3 Rao et al. [44] proposed a multi-objective optimization of supercritical carbon dioxide
4 recompression Brayton cycles that resulted in an efficiency ranging from 43 to 53.8%.
5 Further studies should quantify the heat losses associated with the particle conveying and the
6 parasitic power consumption due to fluidization air in both the solar receiver and the heat
7 exchanger. Besides, a techno-economic assessment, using appropriate economic indicators, is
8 necessary to evaluate the competitiveness of the proposed concept. For example, US DOE
9 2030 cost targets for CSP is 5 c\$ per kilowatt-hour for a baseload plant with 12 or more hours
10 of storage and 10 c\$ per kilowatt-hour for a peaker plant with six or fewer hours of storage
11 [45].

12

13 **7. Conclusion**

14 The design and the performance of a medium-scale flexible solar power plant integrating a
15 combined cycle with a fluidized particle-in-tube receiver and direct thermal storage are
16 presented.

17 To provide practical technical information, a gas turbine with a low TIT has been selected to
18 describe the performance of the solar combined cycle power plant. Besides, the components'
19 performance maps are used to provide the actual performance of the power conversion cycles
20 and a rigorous methodology is employed to design the solar receiver, the heliostat field, and
21 the fluidized bed heat exchanger. Both full-load and part-load performance are evaluated and
22 three cases are investigated: hybrid, solar-only, and solar-only low flowrate.

23 The evaluation of the performance under different operation strategies indicates that the solar
24 power plant provides a great flexibility thanks to the direct energy storage. The analysis of the
25 components and the overall plant efficiencies for typical days shows promising performance

1 during summer, spring, and autumn leading to an annual capacity factor above 33%. The
2 efficiency of the power block reaches 46%. The overall nominal efficiency (solar-to-electric
3 efficiency) of the power plant showed a strong dependence on the optical efficiency of the
4 solar field but a weak function of the receiver's efficiency. It reaches 25.80% for the hybrid
5 case because the solar field is relatively small. For the case of the solar-only, which has a
6 large solar field, the overall efficiency drops to 21.16%. Nevertheless, this latter value can be
7 enhanced up to 24.7% by reducing the power of the collection loop.

8 This paper presents a general methodology for simulating fluidized particles-base solar
9 thermal power plants that can be applied to the integration of different conversion cycles and
10 be used to design large-scale commercial power plants composed of several modules sharing
11 the same power block. Realistic overall performance calculations are provided on the basis of
12 the use of an off-the-shelf gas turbine with known performance. It is shown that even in this
13 case an increase of 10% relative cycle efficiency with respect to current technology is
14 attainable. An increase of 20 to 25% relative cycle efficiency is expected with advanced sCO₂
15 cycles. With respect to overall plant performance, operating a solar receiver at high
16 temperature may result in a decrease of its efficiency with respect to molten salt technology.
17 Nevertheless, this decrease can be limited to about 6% relative (from 90% to 85%, because an
18 optimized design of the particle solar receiver may result in the increase of the thermal
19 efficiency from 83% -Fig. 12- to 85%). Finally, a significant increase of overall solar power
20 plant efficiency with respect to state-of-the-art central receiver technology is expected using
21 the particle technology.

22

23 **Acknowledgments**

24 This work has received funding from the European Union's Horizon 2020 research and
25 innovation program under grant agreement No 727762, Next-CSP project and was supported

1 by the French “Investments for the Future” program managed by the National Agency for
2 Research, under contract ANR-10-LABX-22-01 (labex SOLSTICE).

3

4 **References:**

- 5 [1] Six L., Elkins R. Solar Brayton engine/alternator set. In: Parabolic Dish Solar Thermal
6 Power Annual Program Review, 1981;23–36.
- 7 [2] Mazzonib M., Cerria G., Chennaouia L. A simulation tool for concentrated solar
8 power based on micro gas turbine engines. *Energy Conversion and Management* 2018;174:
9 844–854
- 10 [3] Aichmayer L., Garrido J., Laumert B. Scaling effects of a novel solar receiver for a
11 micro gas-turbine based solar dish system. *Solar Energy* 2018;162:248–264.
- 12 [4] OMSOP (Optimised Microturbine Solar Power system): Final Report Summary.
13 <https://cordis.europa.eu/project/rcn/106967/reporting/es> [accessed 12 October 2019]
- 14 [5] Coventry J., Andraka C. Dish systems for CSP. *Solar Energy* 2017;152:140–170.
- 15 [6] Behar O., Khellaf A., Mohammedi K. A review of studies on central receiver solar
16 thermal power plants. *Renewable and Sustainable Energy Reviews* 2013;23:12–39.
- 17 [7] Heller P., Pfander M., Denk T., Tellez F., Valverde A., Fernandez J., Ring A. Test and
18 evaluation of a solar powered gas turbine system. *Solar Energy* 2006;80:1225–1230.
- 19 [8] Schwarzbozl P., Buck R., Sugarmen C., Ring A., Crespo M., Altwegg P., Enrile J.
20 Solar gas turbine systems: Design, cost and perspectives. *Solar Energy* 2006;80:1231–1240.
- 21 [9] SOLGATE solar hybrid gas turbine electric power system. Technical Report, 2005.
- 22 [10] Solar-Hybrid Power and Cogeneration Plants (SOLHYCO). Technical report, 2011.
- 23 [11] Quero M., Korzynietz R., Ebertc M., Jiménez A., del Río A., Brioso J.A. Solugas –
24 Operation experience of the first solar hybrid gas turbine system at MW scale. *Energy*
25 *Procedia* 2014;49:1820 –1830.

- 1 [12] Behar O. A novel hybrid solar gas turbine. *Energy Conversion and Management* 2018;
2 158: 120–132.
- 3 [13] Bellos, E., Tzivanidis, C., Antonopoulos, K. A. Parametric analysis and optimization of a
4 solar assisted gas turbine. *Energy Conversion and Management* 2017; 139: 151–165.
- 5 [14] Spelling J. Hybrid Solar Gas-Turbine Power Plants - A Thermo-economic Analysis. Ph.D.
6 thesis, KTH Royal Institute of Technology School of Industrial Engineering and
7 Management, 2013.
- 8 [15] Grange B., Dalet C., Falcoz Q., Ferrière A., Flamant G. Impact of thermal energy storage
9 integration on the performance of a hybrid solar gas-turbine power plant, *Applied Thermal*
10 *Engineering* 2016; 105: 266-275.
- 11 [16] Sánchez-Orgaz S., Medina A., Calvo Hernández A. Recuperative solar-driven multi-step
12 gas turbine power plants. *Energy Conversion and Management* 2013; 67: 171–178.
- 13 [17] Santos, M. J., Merchán, R. P., Medina, A., Calvo Hernández, A. Seasonal
14 thermodynamic prediction of the performance of a hybrid solar gas-turbine power plant.
15 *Energy Conversion and Management* 2016; 115: 89–102.
- 16 [18] Merchán R.P., Santos M.J., Reyes-Ramírez I., Medina A., Hernández A. Modeling
17 hybrid solar gas-turbine power plants: Thermodynamic projection of annual performance and
18 emissions. *Energy Conversion and Management* 2017; 134: 314–326.
- 19 [19] Petrakopoulou, F., Sánchez-Delgado, S., Marugán-Cruz, C., Santana, D. Improving the
20 efficiency of gas turbine systems with volumetric solar receivers. *Energy Conversion and*
21 *Management* 2017; 149: 79–592.
- 22 [19] Korzynietz R., Brioso J.A., del Río A., Quero M., Gallas M., Uhlig R., Ebert M., Buck
23 R., Teraji D., Solugas – Comprehensive analysis of the solar hybrid Brayton plant. *Solar*
24 *Energy* 2016;135: 578–589.

- 1 [10] Ho C. K., Christian J., Yellowhair J., Jeter S., Golob M., Nguyen C., Repole K.,
2 Abdel-Khalik S., Siegel N., Al-Ansary H., El-Leathy A., Gobereit B. Highlights of the high-
3 temperature falling particle receiver project: 2012 – 2016. AIP Conference Proceedings
4 2017;1850: 030027 (); DOI: 10.1063/1.4984370.
- 5 [21] Wu W., Amsbeck L., Buck R., Uhlig R., Ritz-Paal R.. Proof of concept test of a
6 centrifugal particle receiver. Energy Procedia 2014; 49:560 –568.
- 7 [22] CSP2: Concentrated Solar Power in Particles <https://www.csp2-project.eu/>. [accessed
8 12 October 2019]
- 9 [23] Next-CSP: High Temperature concentrated solar thermal power plant with particle
10 receiver and direct thermal storage. <http://next-csp.eu/>. [accessed 12 October 2019]
- 11 [24] Flamant G., Gauthier D., Benoit H., Sans J.L., Garcia R., Boissière B., Ansart R.,
12 Hemati M. Dense suspension of solid particles as a new heat transfer fluid for concentrated
13 solar thermal plants: On-sun proof of concept. Chemical Engineering Science 2013;102:567–
14 576.
- 15 [25] Le Gal A., Grange B., Tessonnaud M., Perez A., Escape C., Sans J-L., Flamant G.
16 Thermal analysis of fluidized particle flows in a finned tube solar receiver. Solar Energy
17 2019;191:19–33
- 18 [26] Zhang H.L., Benoit H., Gauthier D., Degreve J., Baeyens J., Perez Lopez I., Hemati
19 M., Flamant G. Particle circulation loops in solar energy capture and storage: gas-solid flow
20 and heat transfer considerations. Applied Energy 2016;161:206-224.
- 21 [27] Farsi A., Dincer I. Thermodynamic assessment of a hybrid particle-based concentrated
22 solar power plant using fluidized bed heat exchanger. Solar Energy 2019;179: 236–248.
- 23 [28] Kang Q., Dewil R., Degrève J., Baeyens J., Zhang H. Energy analysis of a particle
24 suspension solar combined cycle power plant. Energy Conversion and Management
25 2018;163:292–303.

- 1 [29] Buck R., Giuliano S., Solar tower system temperature range optimization for reduced
2 LCOE. AIP Conference Proceedings 2019;2126:030010; <https://doi.org/10.1063/1.5117522>.
- 3 [30] Solar Power Tower Integrated Layout and Optimization Tool (SolarPILOT™).
4 Available at: <https://www.nrel.gov/csp/solarpilot.html> [accessed 20 October 2019]
- 5 [31] Grobler A., Gauché P. A review of aiming strategies for central receiver, 2nd Annual
6 Southern African Solar Energy Conference 2014.
- 7 [32] Salomé A., Chhel F., Flamant G., Ferriere A., Thiery F. Control of the flux
8 distribution on a solar tower receiver using an optimized aiming point strategy: Application to
9 THEMIS solar tower. Solar Energy 2013;94:352–366
- 10 [33] Collado F.J., Gómez A., Turégano J.. An analytic function for the flux density due to
11 sunlight reflected from a heliostat. Solar Energy 1986;37:215-234.
- 12 [34] SOLSTICE, SOLar Simulation Tool In ConcEntrating optics, version 0.7.1 (2017),
13 <https://www.labex-solstice.fr/logiciel-solstice.html>
- 14 [35] Grange B., A. Ferrière, D. Bellard, M. Vrinat, R. Couturier, F. Pra, Y. Fan. Thermal
15 Performances of a High Temperature Air Solar Absorber Based on Compact Heat Exchange
16 Technology. Journal of Solar Energy Engineering 2011;133-3:031004
- 17 [36] Gomez-Garcia F., Gauthier D., Flamant G., Design and performance of a multistage
18 fluidized bed heat exchanger for particle-receiver solar power plants with storage. Applied
19 Energy 2017;190:510-523.
- 20 [37] Çengel Y., Cimbala J.M. Fluid Mechanics Fundamentals and Applications. McGraw-
21 Hill College, 2017, ISBN:1259696537.
- 22 [38] Dixon S.L., Hall C.A. Fluid Mechanics and Thermodynamics of Turbomachinery.
23 Sixth edition, Butterworth-Heinemann, 2014.

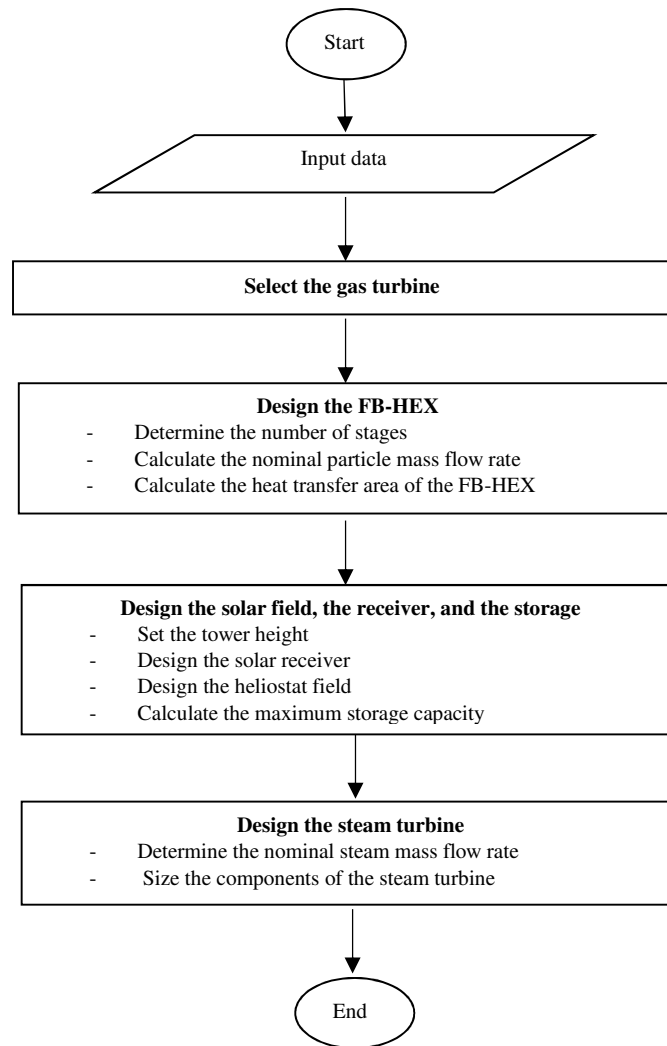
- 1 [39] Semprini S., Sanchez D., De Pascale A. Performance analysis of a micro gas turbine
2 and solar dish integrated system under different solar-only and hybrid operating conditions.
3 *Solar Energy* 2016;132:279–293.
- 4 [40] Horlock J.H. *Advanced gas turbine cycles*. Elsevier Science Ltd, 2003.
- 5 [41] Siemens Gas Turbines (SGT), SGT-500 Industrial Gas Turbine. Available at/
6 http://cfaspower.com/SW_SGT-500.pdf [accessed 13 March 2019].
- 7 [42] Benoit H., Perez Lopez I., Gauthier D., Sans J-L., Flamant G. On-sun demonstration
8 of a 750°C heat transfer fluid for concentrating solar systems: dense particle suspension in
9 tube. *Solar Energy* 2015;118: 622-633.
- 10 [43] Valentin B., Siros F., Brau J-F. Optimization of a Decoupled Combined Cycle Gas
11 Turbine Integrated in a Particle Receiver Solar Power Plant. *AIP Conference Proceedings*,
12 2019; 2126:140007; <https://doi.org/10.1063/1.5117655>.
- 13 [44] Rao Z., Xue T., Huang K., Liao S. Multi-objective optimization of supercritical carbon
14 dioxide recompression Brayton cycle considering printed circuit recuperator design. *Energy*
15 *Conversion and Management* 2019;201:112094.
- 16 [45] [https://www.energy.gov/sites/prod/files/2018/09/f55/Concentrating-Solar-Thermal-](https://www.energy.gov/sites/prod/files/2018/09/f55/Concentrating-Solar-Thermal-Power-FactSheet.pdf)
17 [Power-FactSheet.pdf](https://www.energy.gov/sites/prod/files/2018/09/f55/Concentrating-Solar-Thermal-Power-FactSheet.pdf)

1 **Appendixes:**

2 **Appendix A:**

3 **A.1. Design methodology**

4 The main steps in design the complete solar power plant are illustrated in Figure A.1

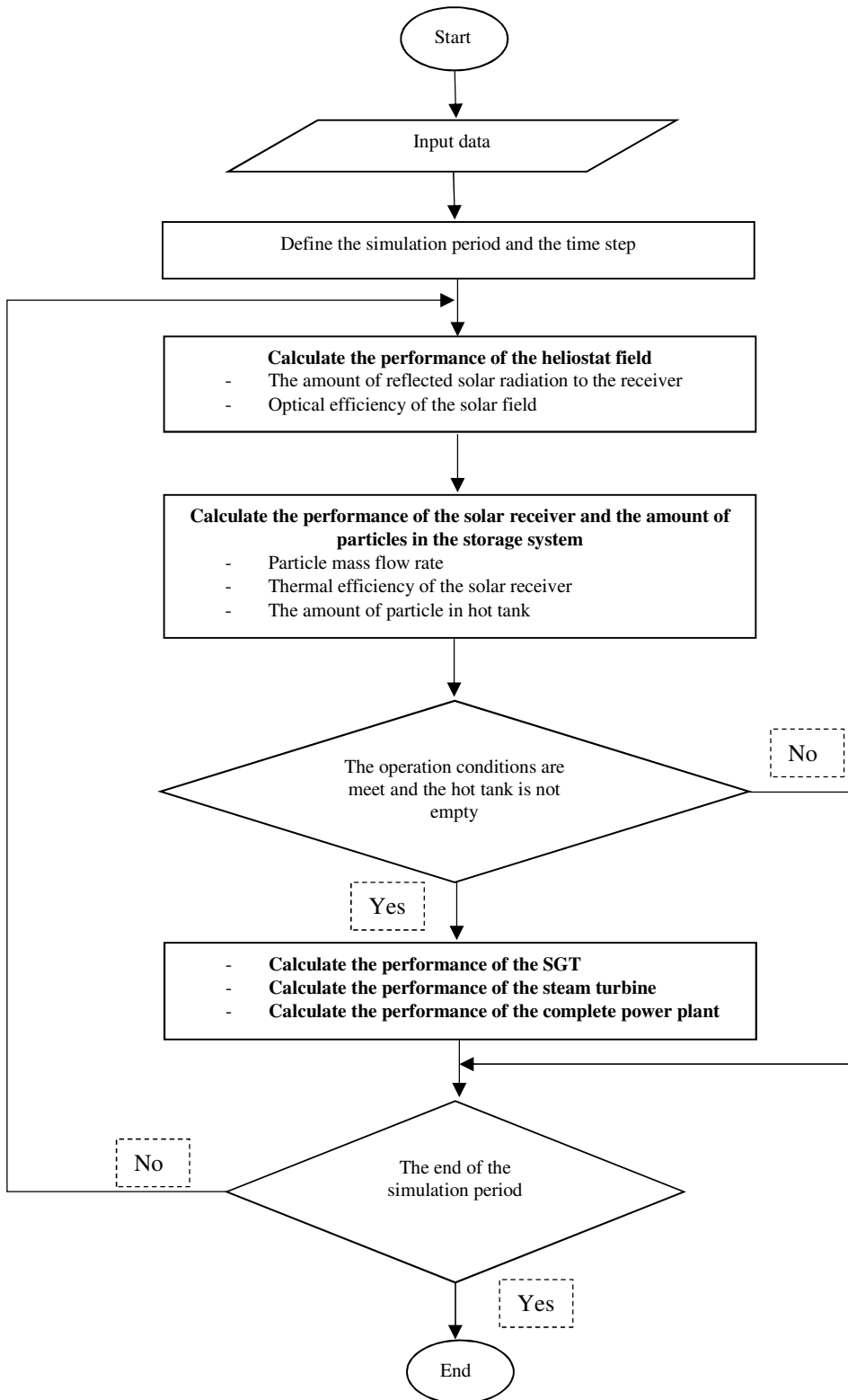


23 Figure A.1. Main steps in the design of solar power plant

24
25
26
27
28
29
30
31

1 **A.2. Performance methodology**

2 Figure A.2 shows the main steps that are used to evaluate the performance of the solar power
3 plant during a typical period.



30 Figure A.2. Main steps in the performance evaluation of solar power plant

$$1 \quad \Delta P_{CDP} = f(N_{rot_CDP}, M_{CDP}) \quad (B2)$$

2 N_{rot} and M are respectively the shaft speed and mass flow rate.

3 The outlet parameters of the CDP including pressure, temperature and enthalpy are calculated
4 as follows. The outlet pressure is obtained by adding the increase in pressure (ΔP) to the inlet
5 pressure (P_{in}).

$$6 \quad P_{out_CDP} = P_{in_CDP} + \Delta P_{CDP} \quad (B3)$$

7 subscripts in and out refer to the inlet, the outlet of the CDP.

8 The actual out enthalpy is calculated based on the concept of isentropic efficiency.

$$9 \quad h_{water_out} = h_{water_in} + \left[\frac{h_{water_out,s} - h_{water_in}}{\eta_{is}} \right] \quad (B4)$$

10 where h and η_{is} refer to the enthalpy and the isentropic efficiency. Subscript s refers to the
11 isentropic enthalpy.

12 The water temperature at the outlet of the pump is calculated as a function of pressure and
13 actual enthalpy.

$$14 \quad T_{water_out} = T(P_{water_out}, h_{water_out}) \quad (B5)$$

15 **B.1.3. Heat Recovery Steam Generator (HRSG)**

16 The HRSG model consists of four sub-programs, i.e., preheater (economizer), evaporator,
17 superheater, and re-heater sub-programs. The input data of the HRSG model are the exhaust
18 gases inlet parameters (mass flow, temperature, and gases composition) as well as water inlet
19 parameters (mass flow, pressure, and temperature).

20 The outlet parameters (water/steam, exhaust gases) are calculated as follows. The outlet
21 pressure of the water/steam is less than that at the inlet due to pressure drop.

$$22 \quad P_{water_out} = P_{water_in} (1 - dp_{water_eco}) \quad (B6)$$

23 dp_{water_eco} is the pressure drop coefficient of cold fluid side (water) in the economizer.

1 To estimate the outlet temperatures of the cold and hot fluids, the NTU-Effectiveness method
 2 has been applied. The actual heat transfer (Q) in the economizer is:

$$3 \quad Q_{eco} = \varepsilon_{eco} \cdot Q_{\max_eco} \quad (B7)$$

4 where: ε_{eco} and Q_{\max} are the effectiveness and the maximum heat transfer of the economizer
 5 respectively.

6 The effectiveness of the economizer is given by,

$$7 \quad \varepsilon_{eco} = \frac{1 - \exp[-NTU \cdot (1 - C_r)]}{1 - C_r \cdot \exp[-NTU \cdot (1 - C_r)]} \quad (B8)$$

8 where: C_r and NTU are respectively the ratio of the heat capacity rates and the Net Transfer
 9 Number of the economizer.

10 At partial loads, the overall heat transfer conductance-area product (UA) is a function of
 11 actual hot fluid mass flow.

$$12 \quad \frac{UA}{UA_{ref}} = \left(\frac{m}{m_{ref}} \right)^{0.8} \quad (B9)$$

13 where: m is the exhaust gases mass flow rate. Subscript ref refers to the design parameter.

14 The actual outlet enthalpy of the cold fluid (water/steam) is calculated as follows,

$$15 \quad h_{cold_out} = h_{cold_in} + \frac{Q_{eco}}{m_{water}} \quad (B10)$$

16 A similar approach has been used to model the evaporator, the super-heater, and the re-heater.

17 **B.1.4. Modeling the HPT and LPT sections**

18 The steam turbine performance map is used for determining the expansion ratio and the
 19 isentropic efficiency as a function of corrected rotational speed and corrected mass flow rates.

20 The same methodology that has been applied for the gas turbine is used herein. The expansion
 21 ratio and isentropic efficiency of the steam turbine are a function of the corrected mass flow
 22 rate and corrected shaft speed.

$$23 \quad \delta_{HPT} = f(N_{cor_HPT}, M_{cor_HPT}) \quad (B11)$$

$$\eta_s^{HPT} = f(N_{COR_HPT}, M_{COR_HPT})$$

(B12)

The pressure at the outlet of the steam turbine section is then obtained.

$$P_{out_HPT} = \frac{P_{in_HPT}}{\delta_{HPT}} \quad (B13)$$

In order to calculate the actual enthalpy at the outlet of the turbine section, the concept of isentropic efficiency is used.

$$\eta_s^{HPT} = \frac{h_{steam_in} - h_{steam_out}}{h_{steam_in} - h_{steam_out_s}} \quad (B14)$$

$h_{steam_out_s}$ is the enthalpy that would have obtained at the outlet of the steam turbine section if the expansion process is isentropic. This ideal enthalpy is evaluated using the outlet pressure and inlet entropy of the steam.

$$h_{steam_out_s} = h(P_{steam_out}, S_{steam_in}) \quad (B16)$$

So that the actual enthalpy is,

$$h_{steam_out} = h_{steam_in} + [\eta_s^{HPT} (h_{steam_in} - h_{steam_out_s})] \quad (B17)$$

The water/steam temperature at the outlet of the steam turbine section is then calculated as a function of pressure and actual enthalpy.

$$T_{steam_out} = T(P_{steam_out}, h_{steam_out}) \quad (B18)$$

The steam fraction is also estimated as a function of pressure and actual enthalpy.

$$X_{steam_out} = T(P_{steam_out}, h_{steam_out}) \quad (B19)$$

A similar approach has been used to model the Low-Pressure Turbine.

B.1.5. Modeling the condenser (CD)

An air-cooling condenser is considered. The model of the condenser is similar to that of the evaporator. The inlet parameters of the condenser model are the outlet parameters of the LPT.

B.2. Design of the Rankine steam cycle

1 The Rankine steam cycle is designed based on the temperature and the mass flow rate of the
 2 GT's exhaust gases. The difference between the parameters of the exhaust gases in the case of
 3 hybrid and solar modes are minor (solar mode: 80.73 kg/s, 386.96°C, hybrid mode: 79.45
 4 kg/s, 887.27°C). Thus, the solar-mode is taken as a reference to size the components of the
 5 steam turbine.

6 The design has been carried out as follows. First, the nominal inlet pressure of the High-
 7 Pressure Turbine section (HPT) is selected based on the technical data of commercial steam
 8 turbines. A temperature approach (at the outlet of the superheated) of 10°C and a pinch
 9 temperature of 5°C is considered for the design of the HRSG. The full design input data are
 10 summarized in Table B.1.

11 Table B.1. Input data of the design of the steam cycle

Design data	Value	Unit
Mass flow rate of the exhaust gases	80.73	kg/s
Temperature of the exhaust gases	386.96	°C
Inlet pressure of the high-pressure steam section	100	Bar
Re-heat pressure	4	Bar
Approach temperature at the outlet of the HRSG	10	°C
Pinch point	5	°C
Temperature approach at the outlet of the pre-heater	5	°C
Heat loss factor	1	%
Nominal shaft speed the steam turbine	3000	Rpm
Nominal isentropic efficiency of the HPT	0.87	
Compressor working pressure	7000	Pa
Nominal isentropic efficiency of the LPT	0.87	
Nominal shaft speed the condenser pump	3000	Rpm
Nominal isentropic efficiency of the condenser pump	0.8	
Mechanical efficiency of the turbine and the pump	99	%
Electrical efficiency of the turbine and the pump	99	%

12
 13 e-NTU method to used to size the heat exchangers of the HRSG as well as the re-heater. The
 14 pressure drop in the heat exchanger is neglected and a heat loss factor of 1% is considered.
 15 The water/steam mass flow rate is then calculated based on the energy balance of the HRSG.
 16 The re-heater is supposed to be installed at the outlet of the HRSG (after the pre-heater) so

1 that to recover as much as possible heat from the exhaust gases. To do so, a re-heat pressure
2 of 4 bars is chosen. An air condenser is chosen because it is more suitable for a desert climate.
3 The condenser working pressure is selected based on the commercial steam turbines. The
4 performance maps of the HPT, low-pressure turbine (LPT) and the condenser pump are then
5 generated. A modular modeling approach is used to link the models' components (HRSG, re-
6 heater, HPT, LPT, condenser pump, and condenser) together and to find the nominal
7 operation parameters. A sliding pressure strategy is used to control the steam turbine
8 operation. Tables B.2 illustrates the size of the components as well as the nominal operation
9 parameters of the steam cycle.

10
11
12
13
14
15
16
17
18
19
20
21
22
23
24
25
26
27
28
29

1
2
3

Table B.2. Size and nominal performance of steam turbines' components

Design data	Value	Unit
Preheater		
Effectiveness	0.9638	-
NTU	3.8636	-
UA	69.0561	W/K
Evaporator		
Effectiveness	0.8446	-
NTU	1.8618	-
UA	172.5931	W/K
Super-heater		
Effectiveness	0.8681	-
NTU	2.2801	-
UA	40.7185	W/K
Re-heater		
Effectiveness	0.7907	-
NTU	1.7939	-
UA	40.7972	W/K
Air condenser		
Effectiveness	0.7916	-
NTU	1.5683	-
UA	786.9484	W/K
Air mass flow rate	493.7842	kg/s
Other data		
Steam mass flow rate	3.9571	kg/s
Inlet temperature of the HPT	377	°C
Inlet temperature of LPT	224.14	°C
Steam turbine thermal efficiency	32.35	%

4

Graphical Abstract:

